Journal Pre-proof

Analysis of fault bend folding kinematic models and comparison with an analog experiment

Berenice Plotek, Cecilia Guzmán, Ernesto Cristallini, Daniel Yagupsky

PII: S0191-8141(21)00040-7

DOI: https://doi.org/10.1016/j.jsg.2021.104316

Reference: SG 104316

To appear in: *Journal of Structural Geology*

Received Date: 19 November 2020

Revised Date: 24 February 2021

Accepted Date: 1 March 2021

Author statement

Plotek: Conceptualization, Methodology, Software, Validation, Formal analysis, Investigation, Data Curation, Writing - Original Draft, Writing - Review & Editing.

Guzmán: Conceptualization, Methodology, Formal analysis, Investigation, Writing - Original Draft, Writing - Review & Editing.

Cristallini: Methodology, Software, Validation, Formal analysis, Investigation, Data Curation, Supervision, Project administration, Funding acquisition, Writing - Original Draft, Writing - Review & Editing.

Yagupsky: Software, Formal analysis, Writing - Review & Editing.

Analysis of fault bend folding kinematic models and comparison with an analog experiment.

Berenice Plotek[a]*; Cecilia Guzmán[a], Ernesto Cristallini[a,b], Daniel Yagupsky[a].

a Laboratorio de Modelado Geológico (LaMoGe), Instituto de Estudios Andinos "Don Pablo Groeber" (IDEAN), Departamento de Ciencias Geológicas, Facultad de Ciencias Exactas y Naturales, Universidad de Buenos Aires-CONICET. E mail address: bereplotek@gmail.com, ceciliagguzman@hotmail.com, daniely@gl.fcen.uba.ar. Postal Address: Intendente Guiraldes 2160, Ciudad Autónoma de Buenos Aires -C1428EHA, Argentina.

b CONICET - LaTe Andes S.A. E mail address: ecristallini@gmail.com. Postal Address: Las Moreras 51, Vaqueros -A4401XBA, Salta, Argentina.

*Corresponding author: +54 11 4576 3400

Keywords:

Kinematic models

Fault-bend folding

Analog model

Particle image velocimetry

Velocity fields

Abstract:

Analog modeling of a flat-ramp-flat fault system was performed and its geometry and displacement field were compared to those of different kinematic models such as classical fault bend folding, fault parallel flow, incline-shear, curvilinear hinge, and backlimb trishear. To obtain the displacement vectors of the analog experiment, a Particle Image Velocimetry was performed. All analyzed kinematic models could explain the general configuration of the fault bend folding. However, only backlimb trishear could represent the geometry, directions of particle displacements, and relations between the displacements' vectors. We propose in this paper that the combination of different asymmetry angles and different apical angles of the backlimb trishear model for each bend in a fault bend fold could be a very versatile and general kinematic model for simulating fault bend folds. Backlimb trishear apical angle can be used to control the shape of the hinges of a fold, while the asymmetry can be used to convolve the velocity of the particles above the fault. Both apical angle and asymmetries different from zero imply thickness changes. Fault bend folds with high inclination forelimbs can be reproduced with high positive asymmetries in the anticline bends of the fault.

1. Introduction

Fault bend folding forms as the result of the movement of a fault block along a non-planar fault surface, which causes the bending of the block and therefore the formation of the fold. This deformation generally occurs in the hanging wall of the fault (Suppe, 1983; Poblet, 2004; Brandes and Tanner, 2014). It is one of the main causes of the folding of the rocks in nature and the object of different types of analog, numerical-mechanical, geometric, and kinematic modeling. Although, mechanical models (either analog or numerical) allow a better understanding of the dynamics of deformation, geometric and kinematic models have a practical utility when constructing complex balanced cross-sections, and that is why they are the target focus of this work. Different geometric and kinematic models (Figure 1) were proposed to simulate fault bend folding (Suppe, 1983; White et al., 1986; Egan et al., 1997; Kane et al., 1997; Cristallini and Allmendinger, 2002), and some of them were implemented in balance cross-section construction software (Contreras, 2002; Cristallini et al., 2021). We use an analog model as a basis to analyze the different kinematic models and to propose variations in the backlimb trishear method (Cristallini and Allmendinger, 2002) that may be useful to simulate flat-ramp-flat fault systems.

"Insert Figure 1 here"

To produce a fault bend fold in our physical model, appropriate analog materials were used to simulate the upper crust. We employed a flexible sugar paste, which allows us to generate the folding. The analysis of a succession of images, using particle-image velocimetry (PIV), provides a digital visual record of the velocity/displacement vectors during the evolution of the structure. In this work, the shape obtained and the displacement field measured in the analog model of fault bend fold are compared with several geometric and kinematic models. Here we show that backlimb trishear is the model that most faithfully reproduces the geometry, directions of particle displacements, and relations between the displacements' vectors in different parts of the fold. We also prove that this method is well suited to replicate structures with high dipping forelimbs and that by modifying the asymmetries of the backlimb trishear model, changes in the dipping of the layers involved during folding can be achieved.

In the following section, we will first review existing geometric and kinematic models. Next, we will present the analog model performed, and finally, we discuss our overall results.

2. Fault bend folding models

The first quantitative model (here considered as classical fault bend folding model: CFBF) describing the geometry and kinematics of fault bend folds was proposed by Suppe (1983) based on conservation of area and thickness of beds during deformation (Figure 1a). Suppe (1983) formulated the equations that determine both the geometry and kinematics for a fold developed over a fault with a single step or break, as well as for more complex folds formed on ramps with different angles, sheared folds, and hybrid structures (Poblet, 2004; Brandes and Tanner, 2014). The initial assumptions applied for the simplest case are that area is conserved and the thickness of the layers is preserved throughout the evolution of the fold (Suppe, 1983). Therefore, the model ensures that bed length in the slip direction remains constant during deformation. The layers are deformed by flexural slip and axial surfaces are always bisectors of bed bendings (Figure 1a). According to this model, the characteristic shape of a fault bend fold consists of a frontal limb with a greater dip than the backlimb, which remains parallel to the fault's ramp. The evolution of simple step fault bend folds corresponds to two perfectly differentiated stages (Suppe, 1983; Poblet, 2004) known as the lifting of the crest and widening of the crest. It is important to notice that, during the first stage, the slip applied to the hanging wall is not all transmitted forward. In Figure 1a, applied slip is indicated as S0 and transmitted slip as S1, so in this model S0 > S1. Suppe (1983) CFBF conserve area (in cross-sections), thickness, and line length during deformation.

The kinematic field that is associated with the model of kink band migration (Suppe, 1983) was presented by Johnson and Berger (1989). The model proposes that within a simple step structure, 3 velocity domains can be defined based on the fault's geometry. Discontinuities separate these domains and are equivalent to the active axial surfaces previously characterized by Suppe (1983). Vectors are parallel to the lower fault plane in the first domain, then parallel to the ramp in the second domain, and in the third domain, they are parallel to the top fault plane. Hardy (1995) contributes to the development of the kinematic analysis of fault bend folds, describing the horizontal and vertical components of the velocity vectors relying on trigonometric relationships that consider the ramp's dip. Just as in the kink band model the most important operating mechanism is flexural slip (Suppe, 1983; Medwedeff and Suppe, 1997), other models rely on different mechanisms for folding.

One of the most commonly used is the fault parallel flow (FPF in this work) proposed by Egan et al. (1997) and Kane et al. (1997). This model (Figure 1b) is based on migration parallel to the fault of the materials of the hanging wall, using axial surface bisectors of fault bends as limits between different velocities. This method states that all particles within the hanging wall move parallel to the fault surface, along virtual flow paths (Ziesch et al., 2014). Subsequent studies on FPF allow calculating the associated deformation in different areas of the structure (Ziesch et al., 2014). Figure 1b shows that slip applied to the hanging wall (S0) is completely transmitted forward: S0 = S1. This model conserves only area (in cross-sections) during deformation; thickness and line length are not preserved (see for example thinning of the forelimb in Figure 1b).

Another mechanism that can operate in kinematic reconstructions of fault bend folding is the simple shear (Gibbs 1983; 1984) and its derivations (White et al., 1986; White, 1992; Yamada and McClay, 2003). Initially, the method assumed that the hanging wall is deformed by simple shear in vertical planes (Gibbs 1983; 1984). As the angle of shear is vertical, the model is referred to as vertical-shear (Figure 1c). Modifications were subsequently developed and the assumption about the inclination of the shear planes to the vertical is removed (White et al., 1986); this is why the model is commonly known as incline-shear (ISh in this work), where vertical-shear is a special case. The direction of simple shear within the hanging wall block is constant and has a very strong influence on the shape of the resulting fold (White et al., 1986; White, 1992). The slip applied to the hanging wall could be amplified, conserved, or reduced depending on the shear angle. If the shear angle is vertical, the slip is conserved along a complete simple step structure (Figure 1c). This model conserves only area (in cross-sections) during deformation; thickness and line length are not preserved (see for example thinning of backlimb and forelimb in Figure 1c).

The theory initially formulated by Suppe (1983) covers exclusively folds formed from faults composed of straight segments with angular breaks, so the modeled examples fail to mimic the traits observed in natural cases. They fail to reconstruct the curved geometry seen in many of the main faults from which the anticlines are generated (Medwedeff and Suppe, 1997). To achieve this feature, Medwedeff and Suppe (1997) propose a model where the main fault has several segments. The length of each segment is reduced, so the fault can be recreated with curved geometry. In this way, the resulting hinge is no longer sharp; on the contrary, it is rounded, which is more consistent with observations from field examples. In turn, each bend generates new axial surfaces that interfere with each other, bringing greater complexity to the structure (Medwedeff and Suppe, 1997). This same idea can also be applied, and simpler, to fault parallel flow and incline-shear models, and is usually used in software cross-section construction. Another modification of the Suppe (1983) CFBF includes the application of basal shear to be able to explain fault bend folds in which backlimb inclination is less than fault dipping (Suppe et al., 2004).

Cristallini and Allmendinger (2002) have pointed out that in several analog and mechanical models of fault bend folding formed above faults composed of straight segments with angular breaks, the resulting fold has rounded hinges. These results cannot be explained by classical fault bend folding, neither by fault parallel flow nor incline-shear. To explain these cases, they propose the backlimb trishear model (BLT in this work; Figure 1e, f, and g; Figure 2) where the fold hinge describes soft curvatures in the upper strata while those layers near the fault zone show strong angular breaks (Cristallini and Allmendinger, 2002). This model conserves only area (in cross-sections) during deformation; thickness and line length are not preserved.

To explain a similar situation, Tavani et al. (2005) replace axial surfaces represented with straight lines by circular zones that generate the curved geometry seen in fold's layers (Figure 1d). This curvilinear hinge model (CH in this paper) conserves area (in cross-sections), thickness, and line length during deformation, and transmits some shear forward. Tavani et al. (2005) model explains rounded anticline hinges, however, cannot explain rounded syncline hinges.

"Insert Figure 2 here"

The backlimb trishear model (Cristallini and Allmendinger, 2002) is conceptually analogous to forelimb trishear (Erslev, 1991, Allmendinger, 1998), and presupposes incompressible flow in triangular zones focused on the fault bends. It uses equations of area conservation, similar to those derived for forelimb trishear by Zehnder and Allmendinger (2000), but in these cases applied to the material above a fault bend. Cristallini and Allmendinger (2002) focused their paper on the backlimb of a fold and named their model as "backlimb trishear" (Figure 2). However, the idea (and of course the equations) can be applied to any bend in a fault and can be used to explain syncline and anticline hinges (Figure 1 e, f, and g). The backlimb trishear, in addition to hanging wall slip and fault bend angle, has basically two variables, the backlimb trishear apical angle, and the asymmetry. The second is measured with respect to the fault bend bisector and is positive forward and negative backward. Cristallini and Allmendinger (2002) showed that a symmetrical backlimb trishear zone does not produce the variation of the applied slip versus the transmitted slip. However, asymmetrical zones produce slip variations. Changing the backlimb trishear asymmetry, the model can satisfy the slip variations of classical fault bend folding (Figure 1e), fault parallel flow (Figure 1f), or incline-shear (Figure 1g).

3. Analog model methodology

Intending to analyze and test different kinematic models of fault bend folding, we perform an analog model to obtain the displacement field during the formation of simple step fault bend folds. In this way, it is possible to evaluate and compare the displacement field and the resulting geometries with those of the investigated kinematic models. The experiment focuses on evaluating the vectors for the first stage of fold growth, where lifting of the crest occurs.

The analog model technique is practical and simple for obtaining displacement fields during deformation. Vectors of displacement are obtained by particle image velocimetry (Sveen, 2004), a methodology widely used in geological process studies (Kincaid and Griffiths, 2003; Boutelier and Cruden, 2013; Strak and Schellart, 2014; Schellart and Strak, 2016) performed with PIVlab-MATLAB program (Thielicke and Stamhuis, 2014). The results obtained were compared with the previously analyzed kinematic models (Figure 1). The technique of analog modeling is useful since it allows the incorporation of a mechanical framework into the kinematic method.

3.1. Analog model setup

To simulate the stage of the lifting of the crest in a simple step fault bend fold, we used an experimental setup consisting of a footwall represented by a rigid, non-deformable wedge and a deformable hanging wall represented by a layered plastic material (Figure 3). To meet the objectives of this experiment, a material that would not fracture or fail was needed. Cohesionless materials as sand, traditionally used in experiments of deformation of the upper crust (Cristallini et al., 2009; Ritter et al., 2016; Marshak et al., 2019), do not meet these characteristics. The models required a cohesive material being able to simulate the strata that constitute a sedimentary cover involved in the folding, where no fractures are desired. For this reason, we used sheets of sugar paste to model the hanging wall. The preparation has a density of 1.27 g/cm^3 and a viscosity equal to 2.2 x 10^7 Pa s, being this value similar to plasticines widely used as analog materials for experimental setups (Schöpfer and Zulauf, 2002; Zulauf and Zulauf, 2004). The sheets are separated from the bottom of the box, the metal wedge, and between them by low friction surfaces. To avoid the formation of voids and to approach the challenging scaling conditions, all the experiment is run inside a biaxial loading cell like that proposed by Bazalgette and Petit (2007). To fill the spaces above the layers of sugar paste, dough made with salt, flour, and water (density □ 1.29 g/cm^3 & viscosity □ 1.2 x 10^5 Pa s) was used. This mass was placed at the top reaching 9 cm in height, separated by a plastic film that acts as a moisture barrier. The dough is used to compress the entire model, increasing vertical pressure over the sugar sheets (Bazalgette and Petit, 2007), and causing the layers of sugar paste to accommodate by folding to the movement of the rigid wedge. As the box is closed, this material allows an increase in the confining stress and thus inhibits the separation of the sugar paste from the fault block.

"Insert Figure 3 here"

To ensure that the deformation occur on top of the wedge, it was decided not to move the hanging wall, as in a classical fault bend fold, but move the footwall wedge instead. The sugar paste layers were cut with different lengths to be in close contact with the ramp of the metal wedge to simulate the fault. However, they cannot be extended to the right side of the experiment because a classical fault bend fold transmits part of the applied slip forward by the upper plane. To simulate this situation, the layers of sugar paste are constructed shorter than the box, and the space that is not occupied by them is filled by a colorless silicone with non-Newtonian behavior with a density of 0.97 g/cm^3 and a viscosity of 5 x 10^4 Pa s at 20° C (Weijermars, 1986). This idea is similar to that used by Chester et al. (1991) in the apparatus to simulate a fault bend fold and is needed to represent this type of structure.

Plane strain condition of the experiment was ensured with continuous observation. The model was photographed on both sides of the deformation box, mounted with two opposite acrylic walls for this purpose. The apparatus also has a motor-driven piston to compress the materials arranged inside. The experiment carried out was 47 cm long by 15 cm wide and 19 cm high (Figure 3). Inside it and in contact with the piston, a rigid wedge of 30° was placed. The wedge is 22 cm long at its base and 14 cm on the upper fault flat and its ramp is 9 cm long. This device simulates the motion of the hanging wall past the fault bends (Zanon and Gomes, 2019). At the base of the experiment, only 25 cm of sugar paste was placed while at the top were placed 37 cm and 10 cm of transparent silicone in contact with the piston (Figure 3). Above the sugar paste and the silicon, the dough was used to fill the box and increase vertical load over the experiment.

The model was compressed for 67 minutes, at 10 cm/hour, reaching a total of 11 cm of shortening and forming a fault bend fold. As the structure is generated, photographs were taken perpendicular to the direction of motion of the piston on both sides of the model to follow the evolution of the fold. Previous trials concluded that the deformation observed through the sidewalls of the box is representative of the internal deformation within the models and plane strain can be assumed. A total of 67 images were obtained, one per minute. These photographs were subsequently processed using the Irfanview TM (Skiljan, 2012) software to crop the area of interest and generate the serial images. These images were analyzed with the PIVlab-MATLAB program (Thielicke and Stamhuis, 2014) to obtain the kinematic vectors that illustrate the displacement field of particles that generate the fold and the evolution during the lifting of the crest.

This experiment is a qualitative analog for a two bend fault bend fold system; it is not an accurately scaled physical model (Hubbert, 1937). It is intended to compare shapes and relative displacement and velocity relations with kinematics models. In this work, we focused on the different domains of the displacement field during the evolution of a fault bend fold rather than the absolute values of the displacement vectors.

3.2. Particle image velocimetry:

There are numerous programs to carry out a particle image velocimetry (Adam et al. 2002, Adam et al., 2005; Schellart and Strak, 2016), but we selected software PIVlab-MATLAB (Thielicke and Stamhuis, 2014) because it is easy to implement and enables complex graphics of both the displacement vectors and their corresponding PIV-derived parameters like the magnitude of displacement velocity (Krýza et al., 2019).

To calculate the vectors this tool divides each of the images into user-defined areas, of a certain number of pixels to be analyzed. The image should be calibrated indicating both the actual distance (in mm) between two points in the photo and the time interval (in ms) between 2 successive photos. In this experiment, each pixel in the photographs represents 0.02 mm of the analog model and the time interval was equal to 60 s. In each defined area, the program compares the pixels for two successive images, detecting differences that are attributable to the movement and plotting the vectors. The presented displacement vectors are calculated on the basis of redistribution of the pixels between the photographs taken 60 s apart, representing the total displacement over that interval. After processing, validation of the vectors is performed, crossing out outliers considering that maximum velocity is the one of the motor-driven piston.

To concentrate the deformation just over the basal ramp, in this experiment the aluminum wedge that represents the footwall of the fault bend fold, worked as a piston, and the hanging wall was passively deformed. Therefore, to compare the results of these experiments with classical fault bend folds, the uniform displacement of the aluminum wedge was subtracted from the obtained vector field. The resultant field was analyzed and plotted in figures 6, 7, and 8.

4. Geometric and kinematic analog model results

4.1. Comparing fold shape

We use the final stage of the analog model to compare the resulting fold shape with those of different kinematic models (Figure 4). The best fit (blue line in Figure 4) was visually made on the yellow highlighted layer of the experiment. Figure 4a compares the analog model with classical fault bend folding (CFBF; Suppe, 1983), Figure 4b with the fault parallel flow model (FPF; Egan et al., 1997; Kane et al., 1997), Figure 4c with a special case of vertically incline-shear, where the inclination of the shear planes is vertical (ISh; White et al., 1986), Figure 4d with curvilinear hinge model (CH; Tavani et al., 2005) and Figure 4e with a special case of backlimb trishear (BLT; Cristallini and Allmendinger, 2002). In a quick view, all the models explain the general geometry of the fold of the analog experiment. However, there are differences, and some models explain better some features than others. For example, CFBF, FPF, and ISh fail to explain the curvilinear shape of the fold, while CH and BLT represent very well this feature for the anticline, but CH does not copy the curvilinear shape of the synclines. ISh model fits very well the area covered by the fold, however, like CFBC, FPF, and CH, it does not fit the slip over the footwall ramp with that of the analog model.

"Insert Figure 4 here"

To analyze backlimb trishear fitting, we tested different trishear apical angles and asymmetries (Figure 5). In the initial code of Cristallini and Allmendinger (2002) both parameters had to be the same for all the fault bendings. In Figure 5 we show the results of different asymmetries, using 30° as trishear apical angle. If we compare the resulting curves with the yellow highlighted bed, we can see that -10° asymmetry works better for the backlimb while +8° asymmetry works better for the forelimb. For this work, we use the development version of Andino 3D software (Cristallini et al., 2020) to modify the original code of Cristallini and Allmendinger (2002) to allow the use of different asymmetries and apical angles for each bend in the fault. In this way, we can produce a better fitting of the yellow highlighted bed using asymmetries of -10° for the backlimb bend and +8° for the forelimb bend (Figure 4e).

"Insert Figure 5 here"

Natural anticlines with flat-ramp-flat geometry, those in which the fault ramp did not broaden to the top but developed an upper flat in the middle of the stratigraphic column can be comparable with our analog model, in particular, if the sedimentary cover involved in the folding does not develop major secondary faults.

4.2. Comparing displacements and velocities

To trace the movement of the particles in the experiment, we use PIVlab-MATLAB (Thielicke and Stamhuis, 2014). The results can be seen in Figure 6 for three steps with 1.25, 2.5 cm, and 4.8 cm of applied slip. The blue vectors in figures 6a, b and c show the incremental displacement field calculated by the PIV. According to the kinematic field, two domains of rotation defining triangular geometries can be recognized, and the movement of particles is concentrated inside them. Figures 6d, e, and f are color maps of the slip vectors direction for the corresponding displacement field; a progressive rotation along the fault bending zone is outlined. The yellow dashed lines of Figure 6 represent the backlimb trishear zones adjusted to the analog model. These triangular zones fit very well the distortion zones seen in the displacement field (Figure 6). The displacement vectors are initially composed of a single horizontal component, Vx. When particles reach the backlimb rotation zone, the vertical component of the displacement vectors increases as the experiment progresses (Figures 6d, e, and f). After that, the displacement vectors remain rather parallel to the surface of the ramp (metal wedge), until particles enter the forelimb rotation zone where they progressively lose the vertical component Vy. Finally, displacement vectors are composed once again by horizontal vectors. The displacement vectors above the ramp are rather parallel to it (Figures 6a and 6b). In advanced stages of the model, the displacement vectors are not completely parallel to the fault, having an angle slightly bigger (Figure 6c). This happens perhaps, because in the final stage of the experiment, the resulting structure, moves a little away from a theoretical fault bend fold, and a smooth lift-off is beginning. Because of this, we considered that the stages represented in figures 6a and b are the most appropriate to make a detailed comparison with a kinematic model.

Figure 7 shows a comparison between the displacement vectors calculated by PIV in the experiment (blue arrows) and those calculated by the backlimb kinematic model using -10° and +8° asymmetries of backlimb and forelimb respectively and an apical angle of 30° (same model as Figure 6b and 6e). There is a very good agreement between both displacement fields, even in the rotation zones above the fault bendings (Figure 7).

"Insert Figure 6 here"

"Insert Figure 7 here"

To compare the mean velocity vectors, three windows of the experiment section were selected to calculate the average velocity magnitudes outside of the triangular areas where vector rotations take place (Figure 8): one over the basal plane (A), one over the ramp (B), and one over the upper plane (C; Figure 8). The average velocities are 6.8 cm/h, 6.19 cm/h and 5.61 cm/h, respectively. In the same figure, a table shows the predicted velocities for the analyzed kinematic models. The decrease in velocity of B with respect to A can only be explained by the backlimb trishear model (BLT) using the same asymmetries as in figures 4e and 7 (backlimb asymmetry -10). The decrease in velocity of C with respect to B can be explained by classical fault bend folding (CFBF), curvilinear hinge model (CH), and backlimb trishear (BLT with +8° of forelimb asymmetry). However, the BLT shows the best fit between the velocity magnitudes.

"Insert Figure 8 here"

To accurately compare the analog model to the different theoretical kinematic models, in Figure 9, we plotted the subtraction of kinematic models velocities to the analog model velocities. Backlimb trishear (BLT) model is the one with the least differences with respect to the analog model, for both the horizontal and vertical components of the velocity vectors (Vx and Vy).

"Insert Figure 9 here"

To facilitate the application of the equation proposed by Cristallini and Allmendinger (2002) to calculate velocity changes across fault bends, we develop the nomogram in Figure 10, where the resultant velocity after a bend can be calculated with respect to a normalized to 1 input velocity

(velocity applied before the bend), the angle between both sections of the fault (φ) and the asymmetry of the backlimb trishear zone (α). The blue curves are for syncline bending of the fault (positives φ), while the orange curves are for anticlinal bendings (negatives φ). The curves for φ = +30° and φ = -30° shown in black are those used for the example of this paper. The blue point corresponds to α = -10° asymmetry of the backlimb adjusted to the experimental fold (Figures 4e and 8) and the red point to the α = +8° asymmetry adjusted to the forelimb (Figures 4e and 8). The resultant velocity V1 is calculated as fractions of the input velocity normalized to 1 (V0 = 1). This means that an output velocity of V1 = 1 implies that there is no change in velocities. Values of V1 < 1 implies a reduction of velocity and V1 > 1 implies an increase. This graph allows sustaining that the BLT model fits the experiment well.

"Insert Figure 10 here"

5. Discussion

The analog simulation described in this work does not represent the generality of the fault bend folds, but it serves to analyze and compare the different kinematic models. We find that all the analyzed kinematic models can broadly explain the fold geometry developed in the experiment (Figure 4). However, backlimb trishear (BLT) is the only one that can mimic accurately the geometry (Figure 4e), directions of particle displacements (Figure 7), and relations between the modulus of the velocity vectors (Figure 8). This is because BLT is the most flexible of the analyzed kinematic models. With the trishear apical angle, the sharpness of the deformation zones above the fault bends can be controlled, while the asymmetries variations can achieve different inclinations of the forelimb and changes in thickness. Moreover, when plotting the slip vectors directions in Figure 6, the change in their angle is gradual and occurs along a triangular shaped rotation zone. These results fit well with the backlimb trishear model (BLT).

Furthermore, by subtracting the vertical and horizontal components of the velocity vector from the fields proposed in theoretical kinematic models from the field obtained for the analog model, the backlimb trishear model (BLT) is the one that presents the smallest differences.

Therefore, it is possible to state that this model is the one that most accurately represents the fold generated in the laboratory and its kinematic evolution. It is postulated that this may be due to the flexibility of the backlimb trishear model (BLT), where a wide range of geometries can be represented from modifications in the aforementioned parameters. The nature of the materials used for the analog model support this conclusion: the sugar paste does not break during deformation, but distributes along the rotation zone presented in BLT model. The same could happen with other cohesive materials such as clay, while coarser granular materials such as dry sand do not develop progressive rotation zones, being probably best represented with other theoretical models.

Cristallini and Allmendinger (2002) focused their work on explaining the geometry of the backlimb in a fault bend fold. However, as we pointed before, their equations are more flexible and can be applied to any bend in the fault surface. We modify their original code to enable the use of independent backlimb trishear apical angles and asymmetries for each bend in the fault. In Cristallini and Allmendinger (2002), the authors compare the BLT model with one of the experiments of Chester et al. (1991). However, they only could compare the backlimb of the fold, because of the limitations of the code. Now, we can show a complete comparison of the same fold (Figure 11). There is a very good fit using a backlimb trishear apical angle of 30° and asymmetries of -10° and +35° for backlimb and forelimb respectively (Figure 11).

"Insert Figure 11 here"

One of the restrictions of geometric and kinematic models of fault bend folding is their ability to represent highly dipping forelimbs. However, this can be solved by adjusting the asymmetry parameter of the BLT model. Figure 12 represents the comparison of one of the models of Chester et al. (1991) with a BLT simulation. In this case, with a forelimb asymmetry of +50, forelimb dipping of 80° can be achieved.

"Insert Figure 12 here"

Finally, based on the analyzes carried out in this work and on cited references, it is clearly observed that most of the described fault bend models (CFBF, FPF, and ISh) imply velocity vectors parallel to the fault, where the only differences are the boundary between domains and the magnitude of the velocity vectors. If we consider the simple step structure as a system of a backlimb fold and a forelimb fold, all these models can be visualized as incline-shear cases, where the field boundaries are in the direction of shear. When the boundary is established symmetrically concerning the fault bend (as a bisector) the velocity magnitudes are conserved. If the boundary is not the bisector of fault bend, the velocity is not preserved on either side of the axial surface. With positive asymmetries, the velocity is incremented after the boundary in a syncline bend and decremented in an anticline bend, while with negative asymmetry the opposite occurs. Fault parallel flow models (FPF) give rise to a symmetrical position of field boundaries with respect to the fault bends and therefore velocities magnitudes are conserved above each fault bend (Figure 1b). In contrast, in the first stage of a classical fault bend folding (CFBF), the axial surfaces are oriented to preserve bedding thickness, and therefore the forward active axial surface does not bisect the fault bend, causing velocity not to be preserved (Figure 1a). For the incline-shear model (ISh), the velocity magnitudes are generally not conserved for each fault bend, and they are incremented or decreased depending on the asymmetry. In the special case of vertical-shear, although the slip is not conserved for each fault bend, it is conserved for the complete system of a simple step structure (Figure 1c). Backlimb trishear (BLT) can be applied to all the previous models (FPF, CFBF, or ISh) just to add progressive rotation to the limbs and to increase the curvilinear geometry of the folds, distributing deformation within a triangular shape shear zone.

Although in this article we were able to simulate a fault bend fold using the BLT model, more work still needs to be done to determine which are the mechanical conditions that control asymmetry and apical angle. Although the discrete-elements model of Hardy and Finch (2007) and the analog models of Bazalgette and Petit (2007) were not made to analyze the BLT, they may suggest that the apical angle depends on the mechanical stratigraphy and friction between beds. With a strongly layered mechanical stratigraphy or very low friction between beds, a parallel layer mechanism is favored and consequently low apical angles in the BLT model. Contrary, the high coupling between beds or a weakly layered mechanical stratigraphy could favor high BLT apical angles. However, these relations need to be demonstrated, and others have to be found concerning the asymmetry. For example, in our experience, the folding above most syncline bends of faults can be described with negative asymmetries in the BLT model, but we have no conclusion about the mechanical causes of this.

6. Conclusions

An analog model made in the laboratory is described and processed to derive a particle image velocimetry. The generated displacement vectors illustrate the migration of materials as a fault bend fold evolves. We use this example as a trigger to analyze different geometric and kinematic models: CFBF (classical fault bed folding), FPF (fault parallel flow), ISh (incline-shear), CH (curvilinear hinge model), and BLT (backlimb trishear). All models can explain the bulk displacements of fault bend folding. However, only BLT can represent the geometry (Figure 4e), directions of particle displacements (Figure 7), and relations between the velocity vector fields (Figure 8).

We propose that the combination of different asymmetry angles and different apical angles of BLT model for each bend in a fault bend fold could be a very versatile and general kinematic model for describing these types of structures. BLT apical angle can be used to control the shape of the hinges of a fold, while the asymmetry can be used to convolve the velocity of the particles above the fault. Both apical angle and asymmetries different from zero imply thickness changes. BLT mode ensures the conservation of area (in a section) during deformation, even when the asymmetry and apical angle are variable for the different bends of the fault. Fault bend folds with high inclination forelimbs can be reproduced with high positive asymmetries in the anticline bends of the fault.

Acknowledgments

Work carried out with the support of a grant from the Agencia Nacional de Promociones Científicas y Técnicas (ANPCyT) PICT project 2016-1407. IDEAN (Instituto de Estudios Andinos

Don Pablo Groeber), Consejo Nacional de Investigaciones Científicas y Técnicas (CONICET), and University of Buenos Aires (UBA) are also recognized for their support during this research. We thank LA.TE. Andes for the academic license of Andino 3D software. The earlier version of this manuscript was greatly improved after constructive comments by Dr. Fernando Hongn and one anonymous reviewer. The fruitful comments of the editor are also appreciated.

References

Adam, J., Urai, J.L., Wieneke, B., Oncken, O., Pfeiffer, K., Kukowski, N., Lohrmann, J., Hoth, S., van der Zee, W., Schmatz, J., 2005. Shear localisation and strain distribution during tectonic faulting - New insights from granular-flow experiments and high-resolution optical image correlation techniques. J. Struct. Geol. 27, 283–301. https://doi.org/10.1016/j.jsg.2004.08.008

Adam, J., Lohrmann, J., Hoth, S., Kukowski, N., Oncken, O., 2002. Strain variation and partitioning in thrust wedges: high-resolution data from scaled sandbox experiments by 2D--3D PIV analysis. Boll. di Geofis. Teor. ed Appl. 42, 123–126.

Allmendinger, R.W., 1998. Inverse and forward numerical modeling of trishear fault propagation folds. Tectonics 17, 640–656. https://doi.org/10.1029/98TC01907.

Bazalgette, L., Petit, J.P., 2007. Fold amplification and style transition involving fractured dip-domain boundaries: Buckling experiments in brittle paraffin wax multilayers and comparison with natural examples. Geol. Soc. Spec. Publ. 270, 157–169. https://doi.org/10.1144/GSL.SP.2007.270.01.11

Boutelier, D., Cruden, A., 2013. Slab rollback rate and trench curvature controlled by arc deformation. Geology 41, 911–914. https://doi.org/10.1130/G34338.1

Brandes, C., Tanner, D.C., 2014. Fault-related folding: A review of kinematic models and their application., Earth-Science Rev. 138, 352-370. https://doi.org/10.1016/j.earscirev.2014.06.008.

Cristallini, E., Hernández, R., Balciunas, D., Nigro, J., Dellmans, M., (2016-2020). Andino 3D Software (1.0.78.0). LATE ANDES 2020.

Cristallini, E., Allmendinger, R., 2002. Backlimb trishear: a kinematic model for curved folds developed over angular fault bends. J. Struct. Geol. 24, 289- 295. https://doi.org/10.1016/S0191-8141(01)00063-3.

Cristallini, E., Tomezzoli, R., Pando, G., Gazzera, C., Martínez, J., Quiroga, J., Buhler, M., Bechis, F., Barredo, S., Zambrano, O., 2009. Controles precuyanos en la estructura de la Cuenca Neuquina. Rev. Asoc. Geol. Argent. 65 (2), 248–264.

Cristallini, E., Sánchez, F., Balciunas, D., Mora, A., Ketcham, R., Nigro, J., Hernández, J., Hernández, R., 2021. Seamless low-temperature thermochronological modeling in Andino 3D, towards integrated structural and thermal simulations. J. South Am. Earth Sci. 105. https://doi.org/10.1016/j.jsames.2020.102851

Chester, J.S., Logan, J.M., Spang, J.H., 1991. Influence of layering and boundary conditions on fault-bend and fault-propagation folding. Geol. Soc. Am. Bull. 103, 1059–1072. https://doi.org/10.1130/0016-7606(1991)103<1059:IOLABC>2.3.CO;2

Contreras, J., 2002. FBF: A software package for the construction of balanced cross-sections. Comput. Geosci., 28(8), 961–969. https://doi.org/10.1016/S0098-3004(02)00019-5

Egan S.S., Buddin T.S., Kane S.J., Williams G.D., 1997. Three-dimensional modelling and visualisation in structural geology: New techniques for the restoration and balancing of volumes. Proceedings of the 1996 Geoscience Information Group Conference on Geological Visualisation - the intelligent picture? Electronic Geology 1, 67-82.

Erslev, E.A., 1991. Trishear fault-propagation folding. Geology 19, 617–620. https://doi.org/10.1130/0091-7613(1991)019<0617: TFPF>2.3.CO;2.

Gibbs, A.D., 1983. Balanced cross-section construction from seismic sections in areas of extensional tectonics. J. Struct. Geol. 5, 153–160. https://doi.org/10.1016/0191-8141(83)90040-8

Gibbs, A.D., 1984. Structural evolution of extension basin margins. J. Struct. Geol. 141, 609–620. https://doi.org/10.1144/gsjgs.141.4.0609

Hardy, S., 1995.A method for quantifying the kinematics of fault-bend folding. J. Struct. Geol. 17, 1785–1788. https://doi.org/10.1016/0191-8141(95)00077-Q

Hardy, S., Finch, E., 2007. Mechanical stratigraphy and the transition from trishear to kink-band fault-propagation fold forms above blind basement thrust faults: A discrete-element study. Mar. Pet. Geol. 24, 75–90. https://doi.org/10.1016/j.marpetgeo.2006.09.001.

Hubbert, M., 1937. Theory of scale models as applied to the study of geologic structures. Bull. Geol. Soc. Am. 48, 1459–1520. https://doi.org/10.1130/GSAB-48-1459

Johnson, A.M., Berger, P., 1989. Kinematics of fault-bend folding. Eng. Geol. 27, 181–200. https://doi.org/10.1016/0013-7952(89)90033-1

Kane, S.J, Williams, G.D., Buddin, T.S., Egan, S.S., Hodgetts, D., 1997. Flexural-slip based restoration in 3D, a new approach. Annual Convention Official Program, American Association of Petroleum Geologists., p. 58.

Kincaid, C., Griffiths, R.W., 2003. Laboratory models of the thermal evolution of the mantle during rollback subduction. Nature 425, 58–62. https://doi.org/10.1038/nature01923

Krýza, O., Závada, P., Lexa, O., 2019. Advanced strain and mass transfer analysis in crustal-scale oroclinal buckling and detachment folding analogue models. Tectonophysics 764, 88–109. https://doi.org/10.1016/j.tecto.2019.05.001.

Marshak, S., Haq, S.S.B., Sen, P., 2019. Ramp initiation in fold-thrust belts: Insight from PIV analysis of sandbox models. J. Struct. Geol. 118, 308–323. https://doi.org/10.1016/j.jsg.2018.11.006.

Medwedeff, D.A., Suppe, J., 1997. Multibend fault-bend folding. J. Struct. Geol. 19, 279–292. https://doi.org/10.1016/s0191-8141(97)83026-x.

Poblet, J., 2004. Geometry and kinematics of bends related to riding. Geology works. 24. 127-146. https://doi.org/10.17811/tdg.24.2004.127-147.

Ritter, M.C., Leever, K., Rosenau, M., Oncken, O., 2016. Scaling the sandbox—Mechanical (dis) similarities of granular materials and brittle rock. J. Geophys. Res. Solid Earth 121, 6863–6879. https://doi.org/10.1002/2016JB012915

Schellart, W.P., Strak, V., 2016. A review of analogue modelling of geodynamic processes: Approaches, scaling, materials and quantification, with an application to subduction experiments. J. Geodyn. 100, 7–32. https://doi.org/10.1016/j.jog.2016.03.009.

Schöpfer, M. P. J., Zulauf, G. 2002. Strain-dependent rheology and the memory of plasticine. Tectonophysics, 354(1-2), 85–99. doi:10.1016/s0040-1951(02)00292-5

Skiljan, I., 2012. IrfanView (4.44). Http:// www.irfanview.com//.

Strak, V., Schellart, W.P., 2014. Evolution of 3-D subduction-induced mantle flow around lateral slab edges in analogue models of free subduction analysed by stereoscopic particle image velocimetry technique. Earth Planet. Sci. Lett. 403, 368–379. https://doi.org/10.1016/j.epsl.2014.07.007

Suppe, J., 1983. Geometry and kinematics of fault-bend folding. Am. J. Sci. 283, 684–721. https://doi.org/10.2475/ajs.283.7.684

Suppe, J., Connors, C.D., Zhang, Y., 2004. Shear fault-bend folding. In: McClay, K.R. (Ed.), Thrust Tectonics and Hydrocarbon Systems AAPG Mem. 82, 303–323.

Sveen, J.K., 2004. An introduction to MatPIV v. 1.6.1. World Wide Web Internet Web Inf. Syst. 27 pp.

Tavani, S., Storti, F., Salvini, F., 2005. Rounding hinges to fault-bend folding: geometric and kinematic implications. J. Struct. Geol. 27, 3–22. https://doi.org/10.1016/j.jsg.2004.07.005.

Thielicke, W., Stamhuis, E.J., 2014. PIV lab – Towards User-friendly, Affordable and Accurate Digital Particle Image Velocimetry in MATLAB. J. Open Res. Softw. https://doi.org/10.5334/jors.bl. J.

Weijermars, R., 1986. Flow behaviour and physical chemistry of bouncing putties and related polymers in view of tectonic laboratory applications. Tectonophysics 124, 325–358. https://doi.org/10.1016/0040-1951(86)90208-8.

White, N., 1992. A method for automatically determining normal fault geometry at depth. J. Geophys. Res. 97, 1715–1733. https://doi.org/10.1029/91JB02565.

White, N.J., Jackson, J.A., McKenzie, D.P., 1986. The relationship between the geometry of normal faults and that of the sedimentary layers in their hanging walls. J. Struct. Geol. 8, 897–909. https://doi.org/10.1016/0191-8141(86)90035-0.

Yamada, Y., McClay, K., 2003. Application of geometric models to inverted listric fault systems in sandbox experiments. Paper 1: 2D hanging wall deformation and section restoration. J. Struct. Geol. 25, 1551–1560. https://doi.org/10.1016/S0191-8141(02)00181-5

Zanon, M.L., Gomes, C.J.S., 2019. Sandbox models of fault-bend folding: A new investigation with a pre-existing fault ramp. J. Struct. Geol 127, 103864. https://doi.org/10.1016/j.jsg.2019.103864

Zehnder, A., Allmendinger, R., 2000. Velocity field for the trishear model. J. Struct. Geol. 22, 1009-1014. https://doi.org/10.1016/S0191-8141(00)00037-7

Ziesch, J., Tanner, D.C., Krawczyk, C.M., 2014. Strain associated with the fault-parallel flow algorithm during kinematic fault displacement. Math. Geosci. 46 (1), 59–73. https://doi.org/10.1007/s11004-013-9464-3.

Zulauf, J., Zulauf, G., 2004. Rheology of plasticine used as rock analog: The impact of temperature, composition and strain. J. Struct. Geol. 26, 725–737. https://doi.org/10.1016/j.jsg.2003.07.005

Figure Captions:

Figure 1: Different geometric-kinematic models for a single step fault bend fold. **a.** Suppe (1983) fault bend folding model (classical fault bend model in this work: CFBF). **b.** Fault parallel flow model (FPF) from Egan et al. (1997). **c.** Incline-shear model (ISh) based on White et al. (1986). In this case, vertical shear indicates that the shear angle of incline-shear model is vertical. **d.** Curvilinear hinge model (CH) from Tavani et al. (2005). **e.**, **f.** and **g.** Backlimb trishear (BLT) from Cristallini and Allmendinger (2002) with asymmetries that satisfy those of CFBF, FPF, and ISh respectively.

Figure 2: a. Backlimb trishear (BLT) implies progressive rotation of the beds over an angular fault bend. The angle 2φ represents the apical angle and V_0 and V_1 the velocities on either side of the triangular zone. θ is the dip angle for the fault. **b.** Definition of the asymmetry angle (α); in (a) triangular zone is symmetric (α=0). Modified from Cristallini and Allmendinger (2002).

Figure 3: Sketch of the experiment pointing out the materials used. The wedge has 30°, simulating the ramp. The dough consists of salt, flour and water. The black arrows indicate the direction and velocity of the moving piston.

Figure 4: Final stage of the hanging wall in the analog model compared to different kinematic models. The best fit (blue line) was visually made on the yellow highlighted layer of the experiment **a.** Suppe (1983) fault bend folding model (CFBF). **b.** Fault parallel flow model (FPF) from Egan et al. (1997). **c.** Incline-shear model (ISh) based on White et al. (1986). **d.** Curvilinear hinge model (CH) from Tavani et al. (2005). **e.** Backlimb trishear (BLT) from Cristallini and Allmendinger (2005). The curvilinear shape of the fold can be only obtained using the curvilinear hinge model or backlimb trishear.

Figure 5: Curves obtained from applying backlimb trishear, using 30° as apical angle and different asymmetries (see figure inset color code). Comparing with the fold shape of the analog model (using the yellow highlighted bed as reference), -10° asymmetry works better for backlimb while +8° asymmetry works better for forelimb.

Figure 6: Total component of the displacement field represented with blue vectors. **a.** Photograph of the experiment with 1.25 cm of applied slip. **b.** Photograph of the experiment with 2.5 cm of applied slip. **c.** Photograph of the experiment with 4.8 cm of applied slip. **d.**, **e.**, and **f.** Color map graphics of slip vectors direction measured anticlockwise from the x-axis. Yellow dashed lines represent the backlimb trishear zones adjusted to the analog model.

Figure 7: Comparison between displacement vectors obtain from the PIV analysis (blue arrows) performed from the serial images of the analog model and those obtained after applying backlimb kinematic model (black arrows) using -10° and +8° asymmetries for backlimb and forelimb, respectively, and an apical angle of 30°. The black dashed lines represent the trishear zones for the backlimb trishear model. Total component of the displacement field represented with blue vectors corresponds to 2.5 cm of applied slip.

Figure 8: **a.** Table presenting different kinematic models and their velocities for the following regions: A. above basal plane. B. above plane over the ramp and C. above the upper plane. Kinematic models used are: classical fault bend folding (CFBF), fault parallel flow (FPF), vertical shear (ISh), curvilinear hinge model (CH) and backlimb trishear (BLT). **b.** Photograph of the experiment with 2.5 cm of applied slip and the total component of the displacement field represented with blue vectors. Yellow dashed lines represent the backlimb trishear zones. White rectangles illustrate the sectors from which the average velocity is calculated.

Figure 9: Resultant from the subtraction of kinematic models velocities to the analog model velocities. Kinematic models used are: classical fault bend folding (CFBF), fault parallel flow (FPF), vertical shear (ISh), and backlimb trishear (BLT) using -10° and +8° asymmetries for backlimb and forelimb, respectively, and an apical angle of 30°. The left column shows the

subtraction of horizontal velocity components (Vx) and the right column, the subtraction of vertical velocity components (Vy). Note that the BLT model is the one with the least differences with respect to the analog model.

Figure 10: a. Scheme showing resultant velocity (V_1) after a fault bend, calculated with respect to a normalized to 1 input velocity (V_0), the angle between both sections of the fault (φ) and the asymmetry of the backlimb trishear zone (α). V_0 and V_1 are the velocities on either side of the triangular zone. φ is the angle between both sections of the fault. α is the angle of asymmetry of the backlimb trishear zone - the angle between the bisector of the fault bend angle (in a fine black straight line) and the bisector of the apical angle of backlimb trishear (BLT axial line, dashed). 1. Syncline bending of the fault (positives φ). 2. Anticlinal bending (negatives φ) (Modified from Cristallini and Allmendinger 2002). **b.** Curves showing resolution for Cristallini and Allmendinger (2002) velocity variation equation. Blue curves are for syncline bending of the fault (positives φ), while the orange curves are for anticlinal bendings (negatives φ). In the analog model, the angle of the fault was 30° (black curves). Blue point corresponds to α = -10° asymmetry of the backlimb adjusted to the experiment fold (Figures 4e and 7). Red point corresponds to the α = +8° asymmetry of the forelimb adjusted to the experiment fold (Figures 4e and 7).

Figure 11: Comparison between analog model from Chester et al. 1991 and a backlimb trishear with 30° of apical angle, α = -10° asymmetry for the backlimb and α = +35° asymmetry for the forelimb.

Figure 12: Backlimb trishear model reconstruction using ANDINO 3D software. The geometry obtained in the analog model with a high dipping forelimb can be reproduced. **a.** Backlimb trishear model with 40° of apical angle, α = -20° asymmetry for the backlimb and α = +50° asymmetry for the forelimb. **b.** Analog model from Chester et al. 1991.

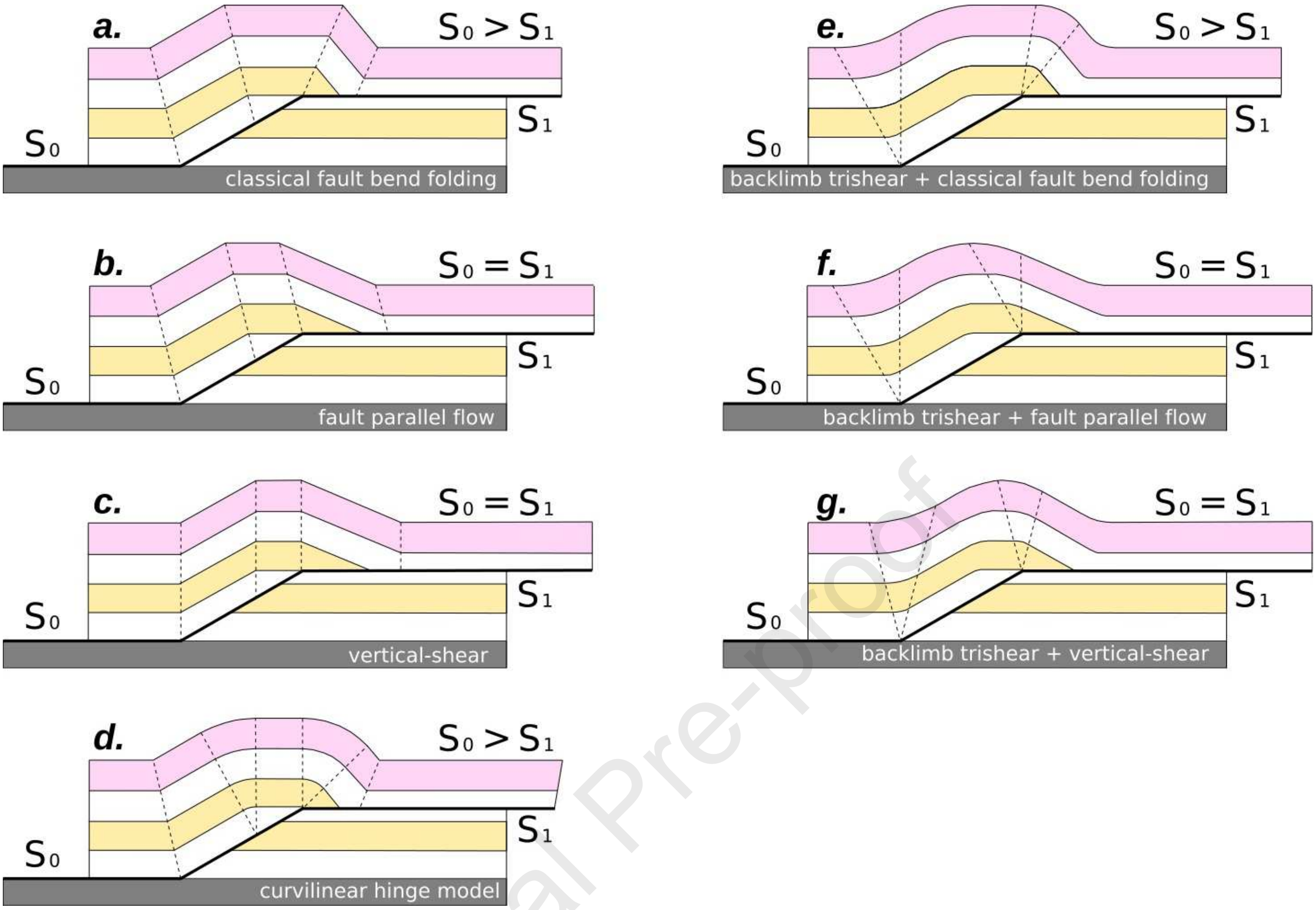

Figure 1: Different geometric-kinematic models for a single step fault bend fold. **a.** Suppe (1983) fault bend folding model (classical fault bend model in this work: CFBF). **b.** Fault parallel flow model (FPF) from Egan et al. (1997). **c.** Incline-shear model (ISh) based on White et al. (1986). In this case, vertical shear indicates that the shear angle of incline-shear model is vertical. **d.** Curvilinear hinge model (CH) from Tavani et al. (2005). **e.**, **f.** and **g.** Backlimb trishear (BLT) from Cristallini and Allmendinger (2002) with asymmetries that satisfy those of CFBF, FPF, and ISh respectively.

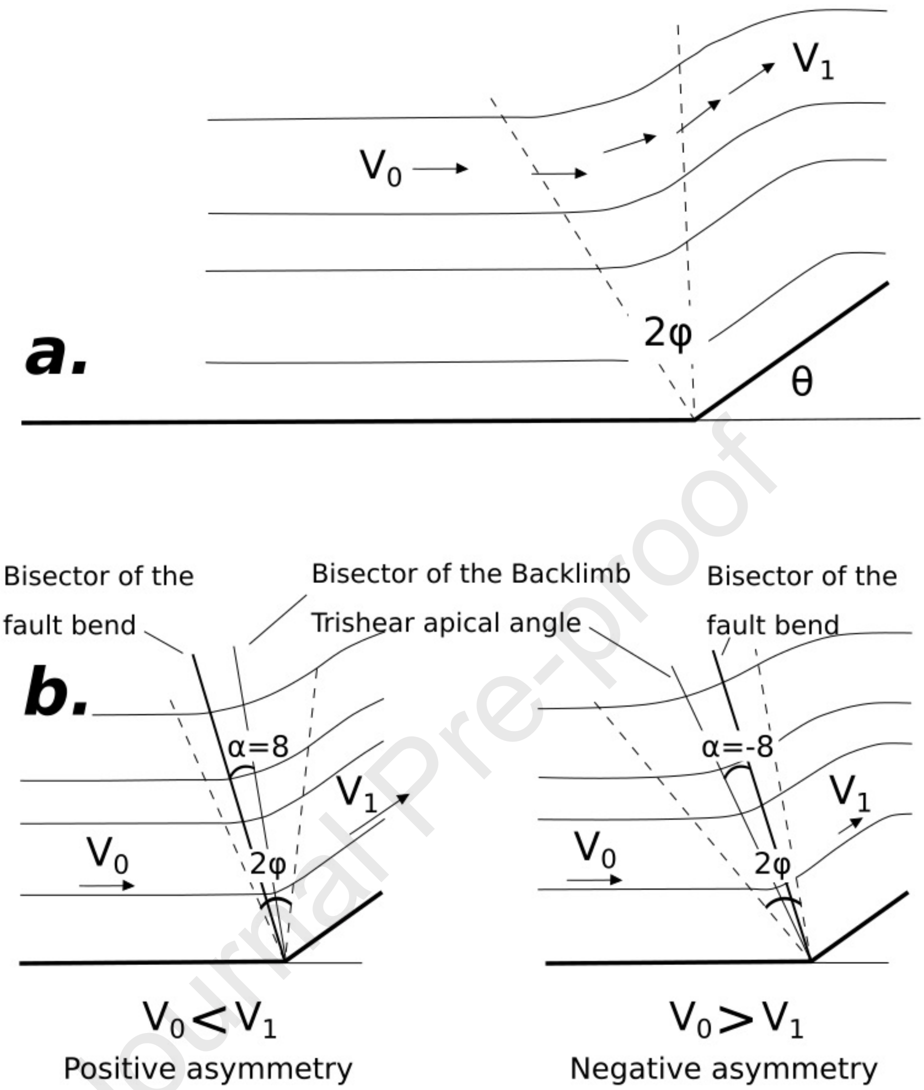

Figure 2: a. Backlimb trishear (BLT) implies progressive rotation of the beds over an angular fault bend. The angle 2φ represents the apical angle and V_0 and V_1 the velocities on either side of the triangular zone. θ is the dip angle for the fault. **b.** Definition of the asymmetry angle (α); in (a) triangular zone is symmetric (α=0). Modified from Cristallini and Allmendinger (2002).

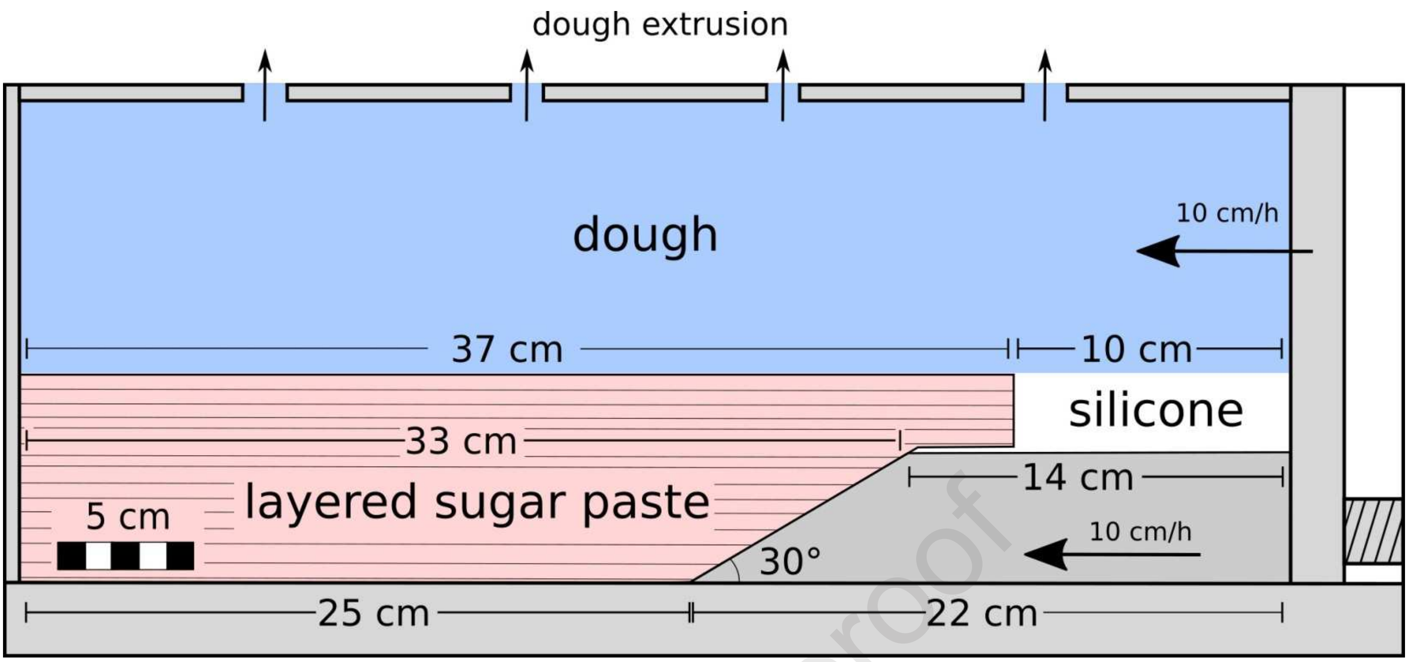

Figure 3: Sketch of the experiment pointing out the materials used. The wedge has 30°, simulating the ramp. The dough consists of salt, flour and water. The black arrows indicate the direction and velocity of the moving piston.

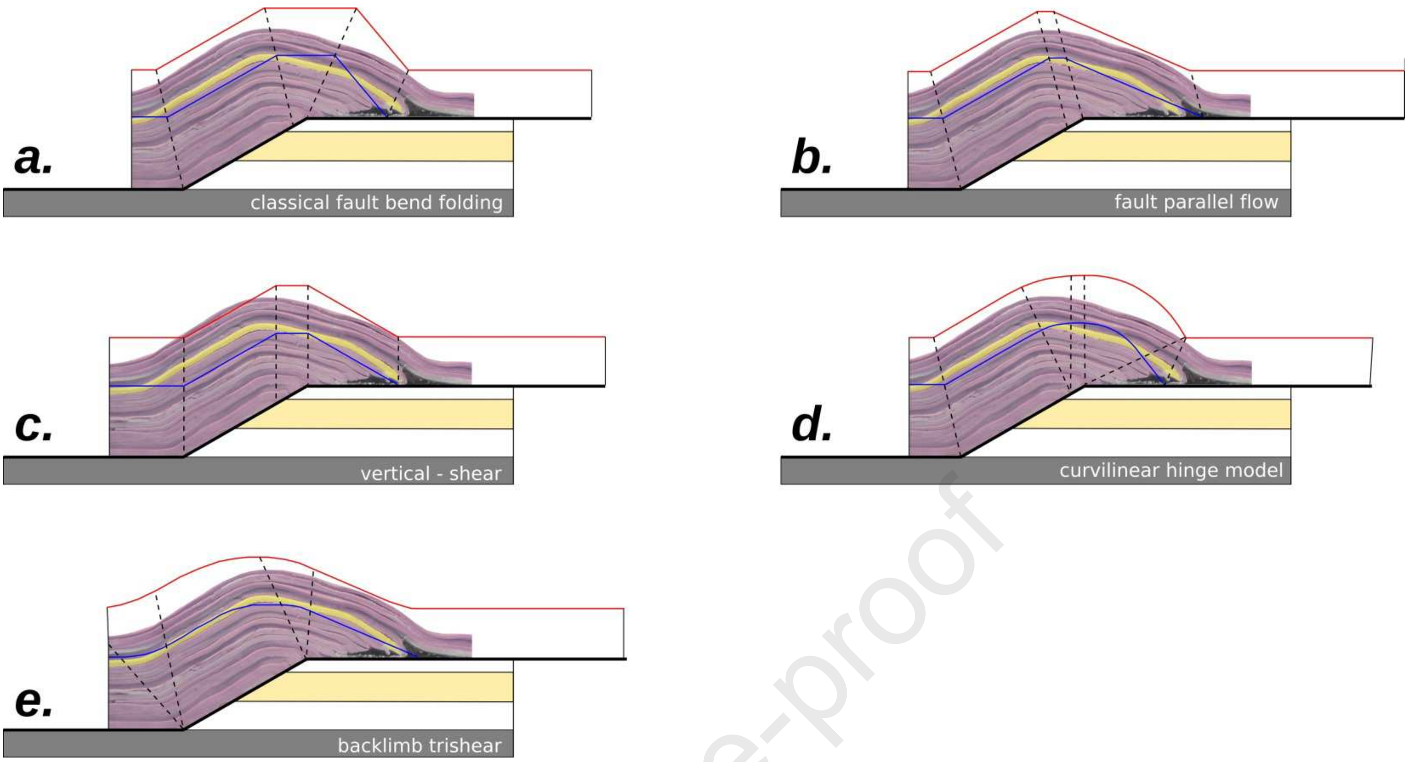

Figure 4: Final stage of the hanging wall in the analog model compared to different kinematic models. The best fit (blue line) was visually made on the yellow highlighted layer of the experiment **a.** Suppe (1983) fault bend folding model (CFBF). **b.** Fault parallel flow model (FPF) from Egan et al. (1997). **c.** Incline-shear model (ISh) based on White et al. (1986). **d.** Curvilinear hinge model (CH) from Tavani et al. (2005). **e.** Backlimb trishear (BLT) from Cristallini and Allmendinger (2005). The curvilinear shape of the fold can be only obtained using the curvilinear hinge model or backlimb trishear.

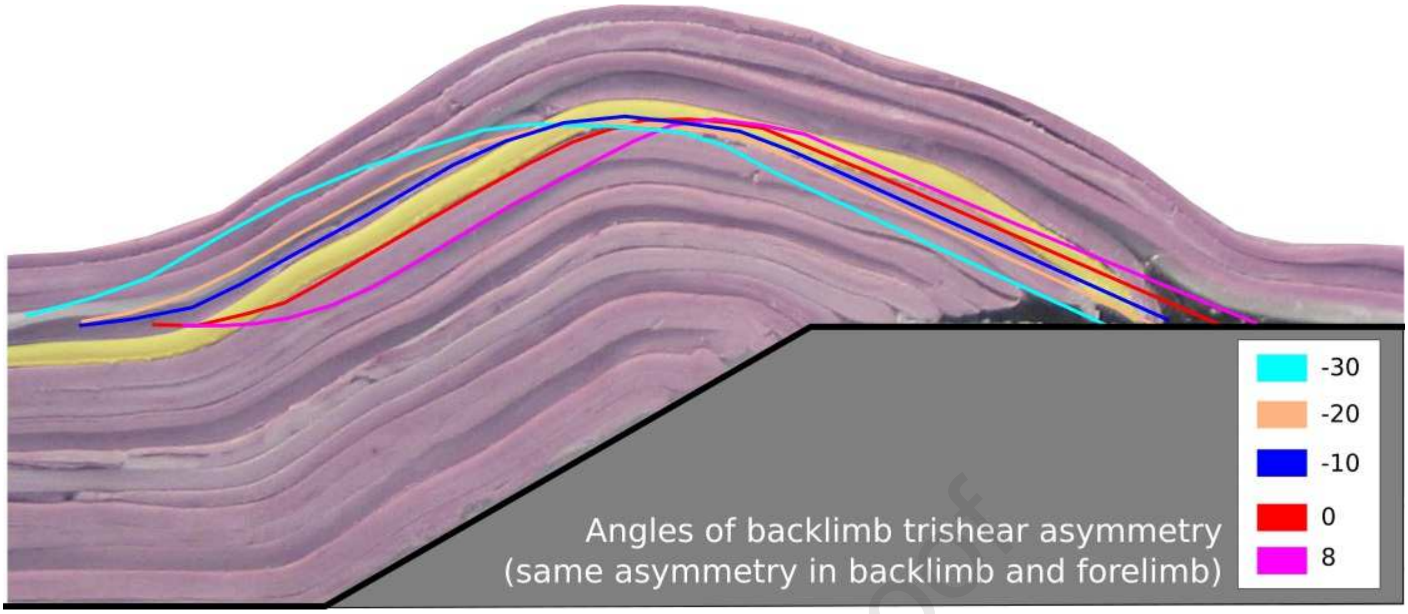

Figure 5: Curves obtained from applying backlimb trishear, using 30° as apical angle and different asymmetries (see figure inset color code). Comparing with the fold shape of the analog model (using the yellow highlighted bed as reference), -10° asymmetry works better for backlimb while +8° asymmetry works better for forelimb.

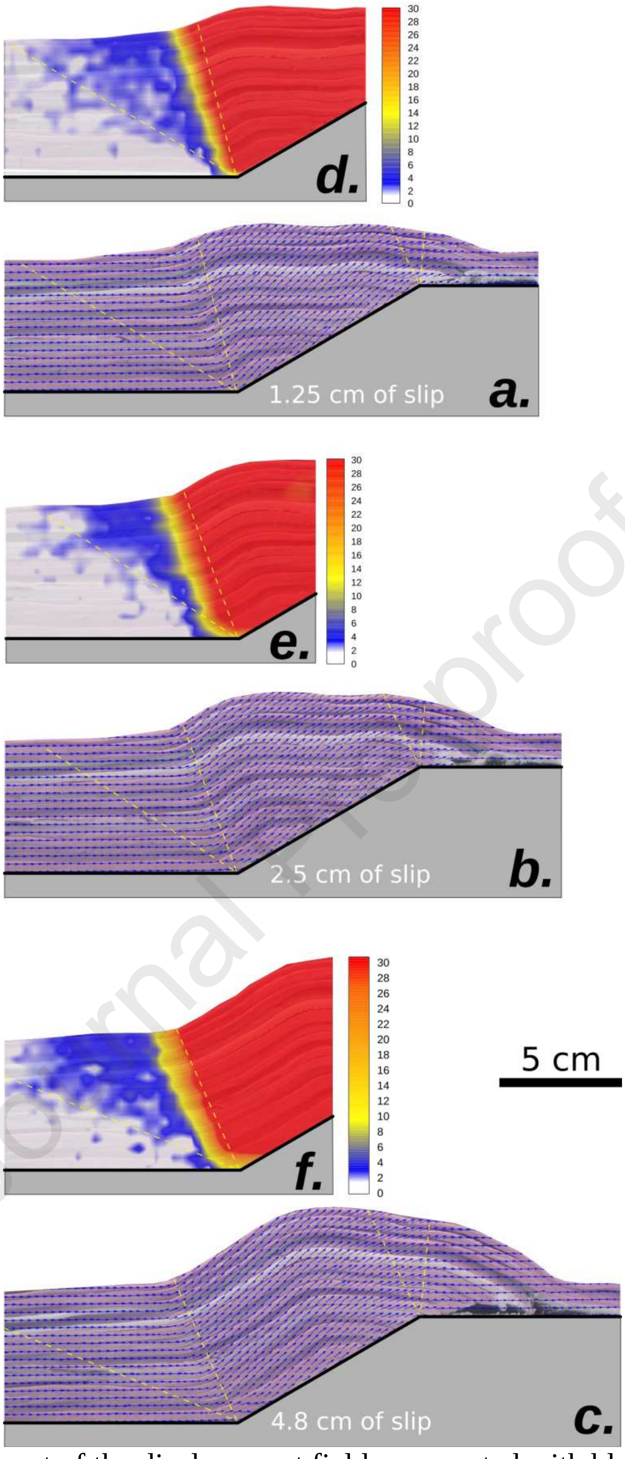

Figure 6: Total component of the displacement field represented with blue vectors. **a.** Photograph of the experiment with 1.25 cm of applied slip. **b.** Photograph of the experiment with 2.5 cm of applied slip. **c.** Photograph of the experiment with 4.8 cm of applied slip. **d.**, **e.**, and **f.** Color map graphics of slip vectors direction measured anticlockwise from the x-axis. Yellow dashed lines represent the backlimb trishear zones adjusted to the analog model.

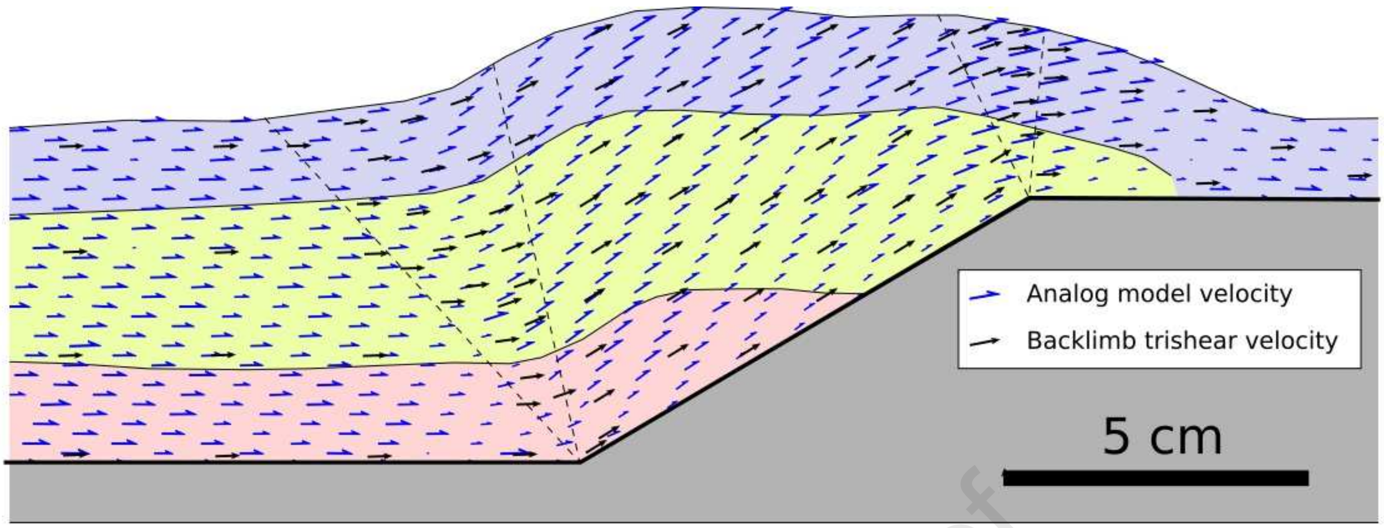

Figure 7: Comparison between displacement vectors obtain from the PIV analysis (blue arrows) performed from the serial images of the analog model and those obtained after applying backlimb kinematic model (black arrows) using -10° and +8° asymmetries for backlimb and forelimb, respectively, and an apical angle of 30°. The black dashed lines represent the trishear zones for the backlimb trishear model. Total component of the displacement field represented with blue vectors corresponds to 2.5 cm of applied slip.

a.

Kinematic model	A (cm/h)	B (cm/h)	C (cm/h)
CFBF	6.8	6.8	3.9
FPF	6.8	6.8	6.8
ISh (vert.)	6.8	7.85	6.8
CH	6.8	6.8	3.9
BLT (-10;+8)	6.8	6.19	5.7

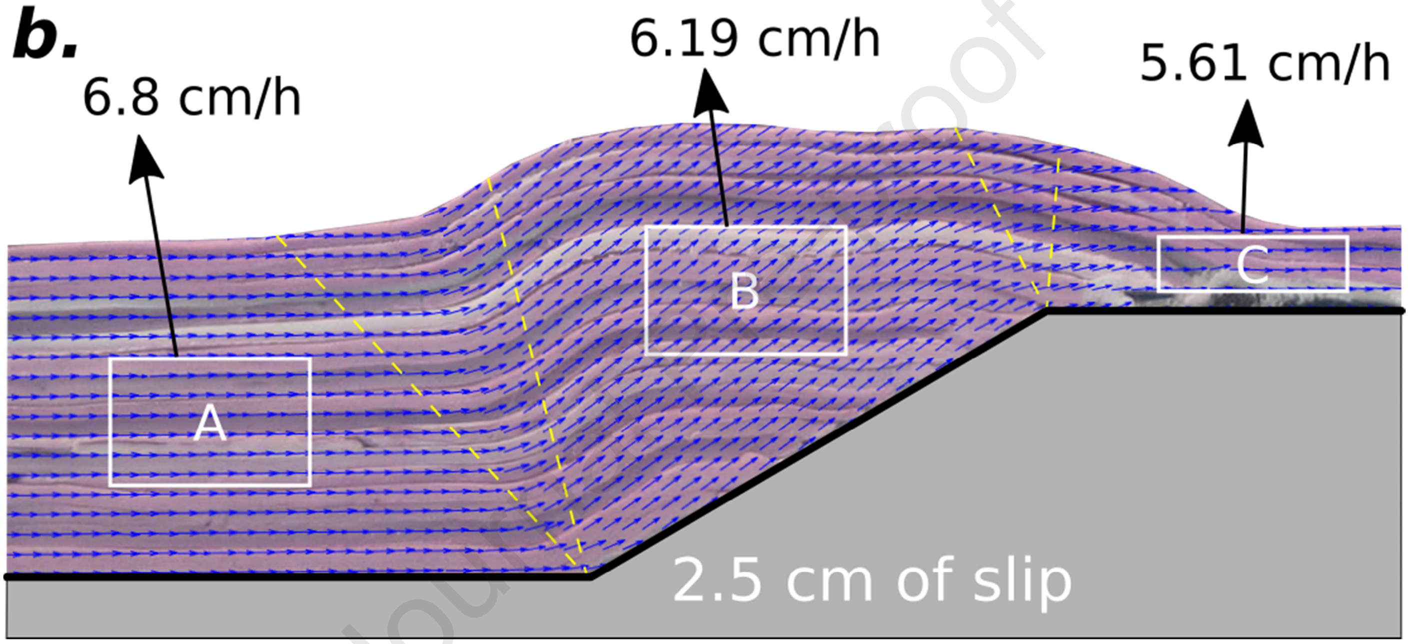

Figure 8: a. Table presenting different kinematic models and their velocities for the following regions: A. above basal plane. B. above plane over the ramp and C. above the upper plane. Kinematic models used are: classical fault bend folding (CFBF), fault parallel flow (FPF), vertical shear (ISh), curvilinear hinge model (CH) and backlimb trishear (BLT). **b.** Photograph of the experiment with 2.5 cm of applied slip and the total component of the displacement field represented with blue vectors. Yellow dashed lines represent the backlimb trishear zones. White rectangles illustrate the sectors from which the average velocity is calculated.

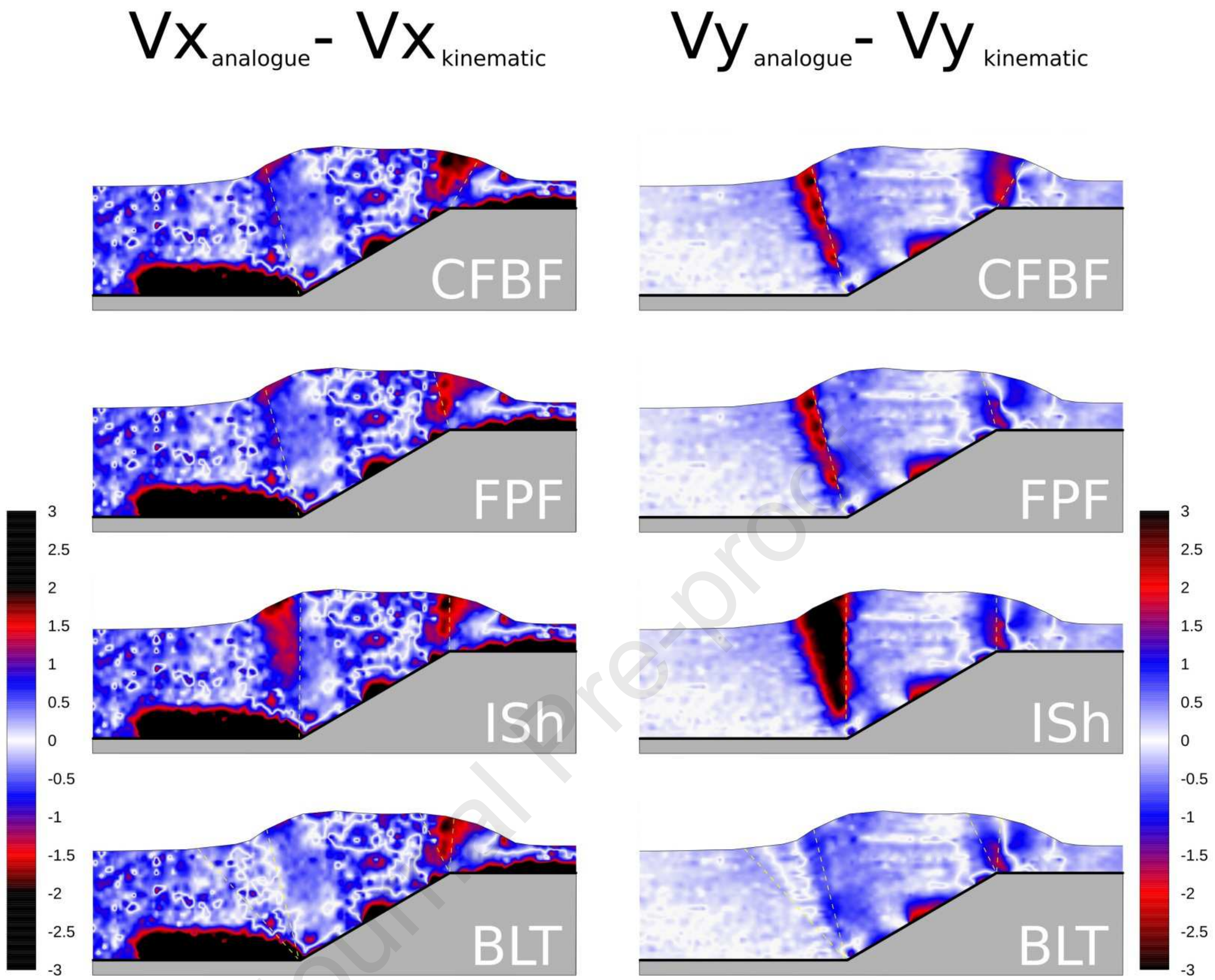

Figure 9: Resultant from the subtraction of kinematic models velocities to the analog model velocities. Kinematic models used are: classical fault bend folding (CFBF), fault parallel flow (FPF), vertical shear (ISh), and backlimb trishear (BLT) using -10° and +8° asymmetries for backlimb and forelimb, respectively, and an apical angle of 30°. The left column shows the subtraction of horizontal velocity components (Vx) and the right column, the subtraction of vertical velocity components (Vy). Note that the BLT model is the one with the least differences with respect to the analog model.

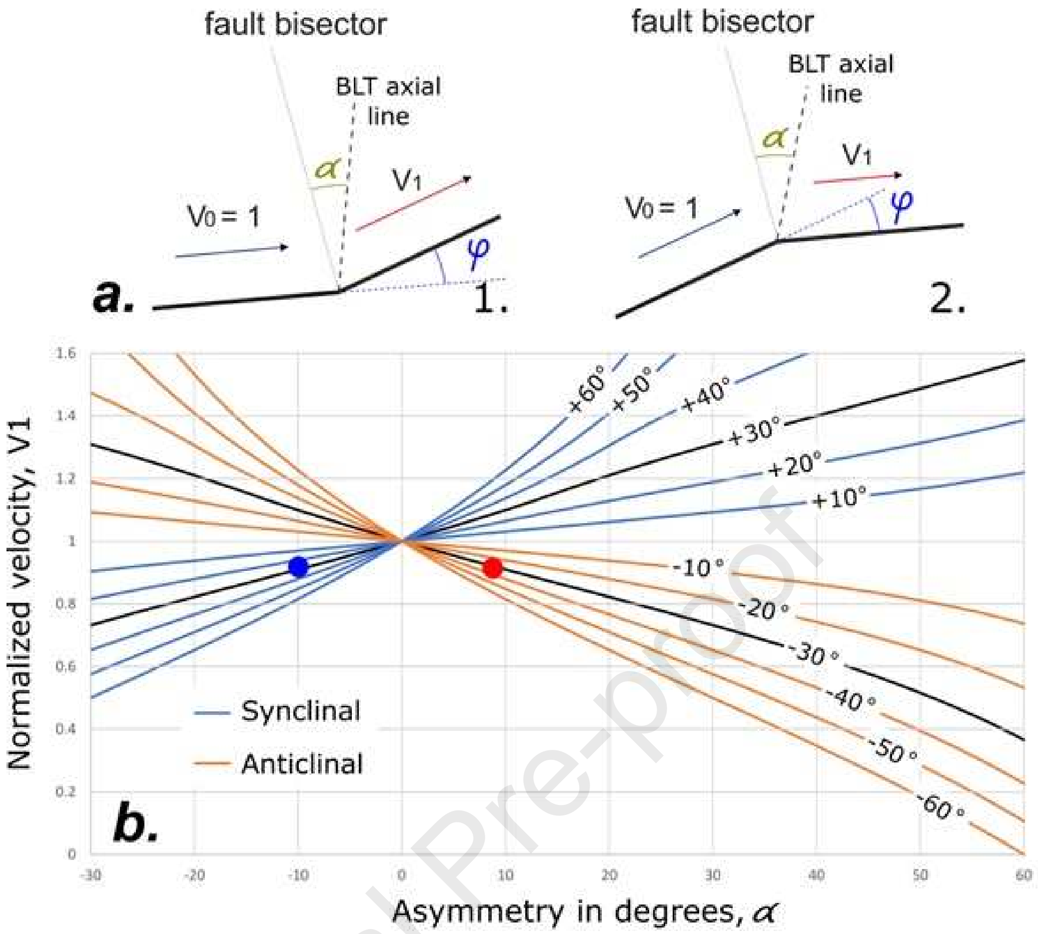

Figure 10: a. Scheme showing resultant velocity (V_1) after a fault bend, calculated with respect to a normalized to 1 input velocity (V_0), the angle between both sections of the fault (φ) and the asymmetry of the backlimb trishear zone (α). V_0 and V_1 are the velocities on either side of the triangular zone. φ is the angle between both sections of the fault. α is the angle of asymmetry of the backlimb trishear zone - the angle between the bisector of the fault bend angle (in a fine black straight line) and the bisector of the apical angle of backlimb trishear (BLT axial line, dashed). 1. Syncline bending of the fault (positives φ). 2. Anticlinal bending (negatives φ) (Modified from Cristallini and Allmendinger 2002). **b.** Curves showing resolution for Cristallini and Allmendinger (2002) velocity variation equation. Blue curves are for syncline bending of the fault (positives φ), while the orange curves are for anticlinal bendings (negatives φ). In the analog model, the angle of the fault was 30° (black curves). Blue point corresponds to α = -10° asymmetry of the backlimb adjusted to the experiment fold (Figures 4e and 7). Red point corresponds to the α = +8° asymmetry of the forelimb adjusted to the experiment fold (Figures 4e and 7).

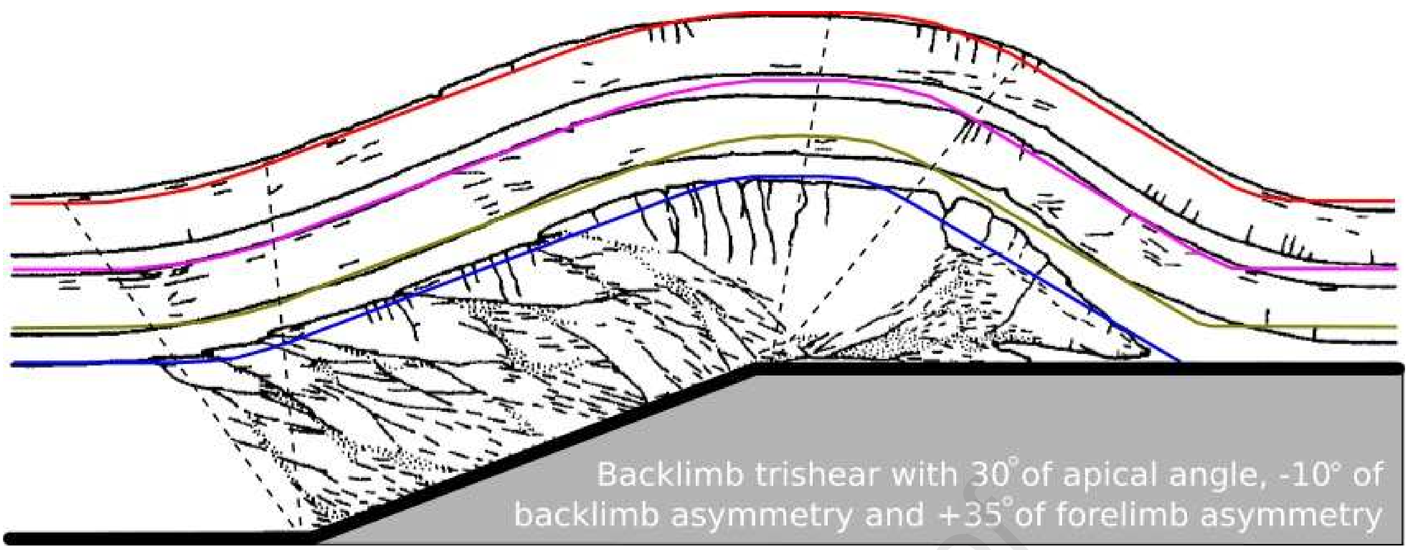

Figure 11: Comparison between analog model from Chester et al. 1991 and a backlimb trishear with 30° of apical angle, α = -10° asymmetry for the backlimb and α = +35° asymmetry for the forelimb.

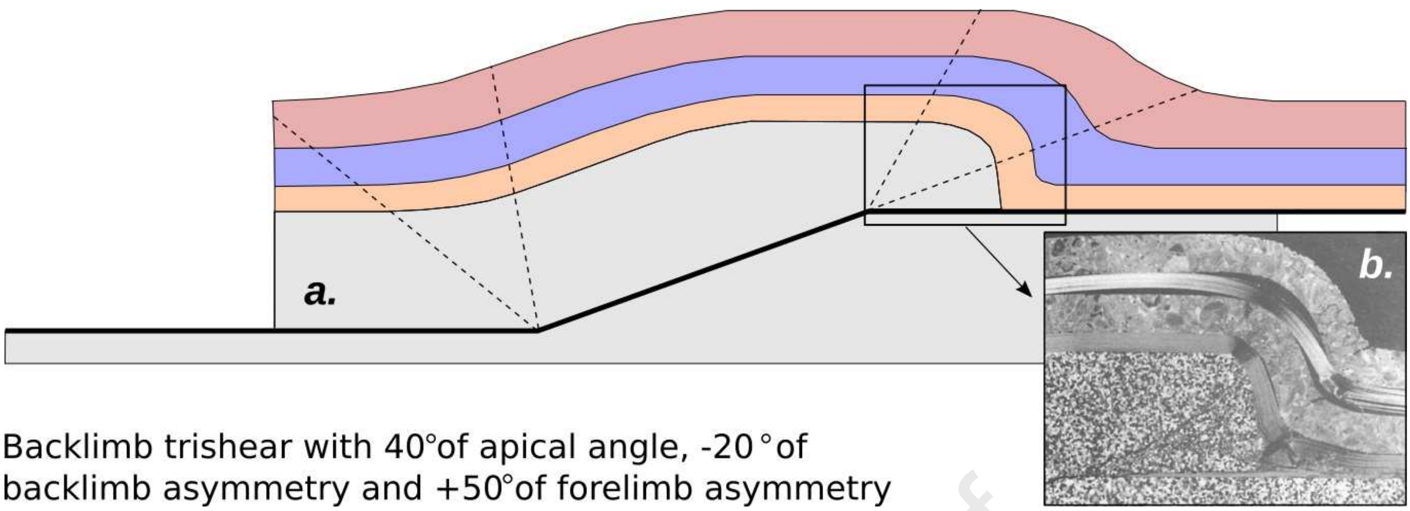

Figure 12: Backlimb trishear model reconstruction using ANDINO 3D software. The geometry obtained in the analog model with a high dipping forelimb can be reproduced. **a.** Backlimb trishear model with 40° of apical angle, α = -20° asymmetry for the backlimb and α = +50° asymmetry for the forelimb. **b.** Analog model from Chester et al. 1991.

Black and white versions:

Figure 1

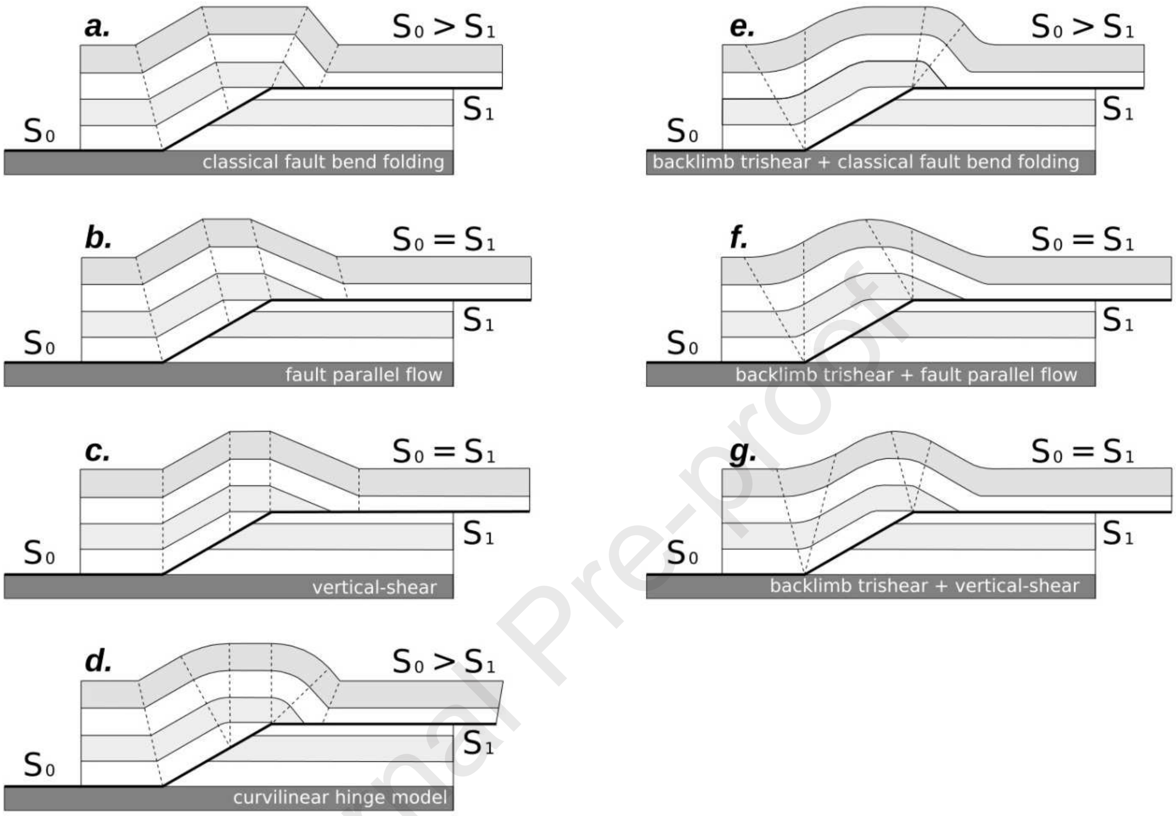

Figure 3

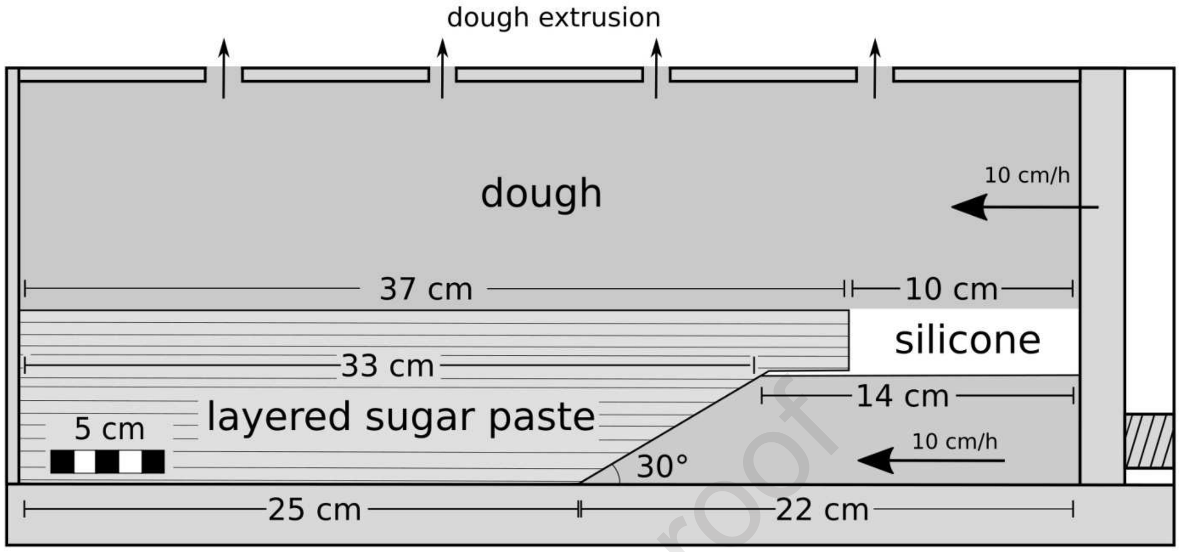
dough extrusion
dough
10 cm/h
37 cm
10 cm
silicone
33 cm
14 cm
layered sugar paste
5 cm
10 cm/h
30°
25 cm
22 cm

Figure 4

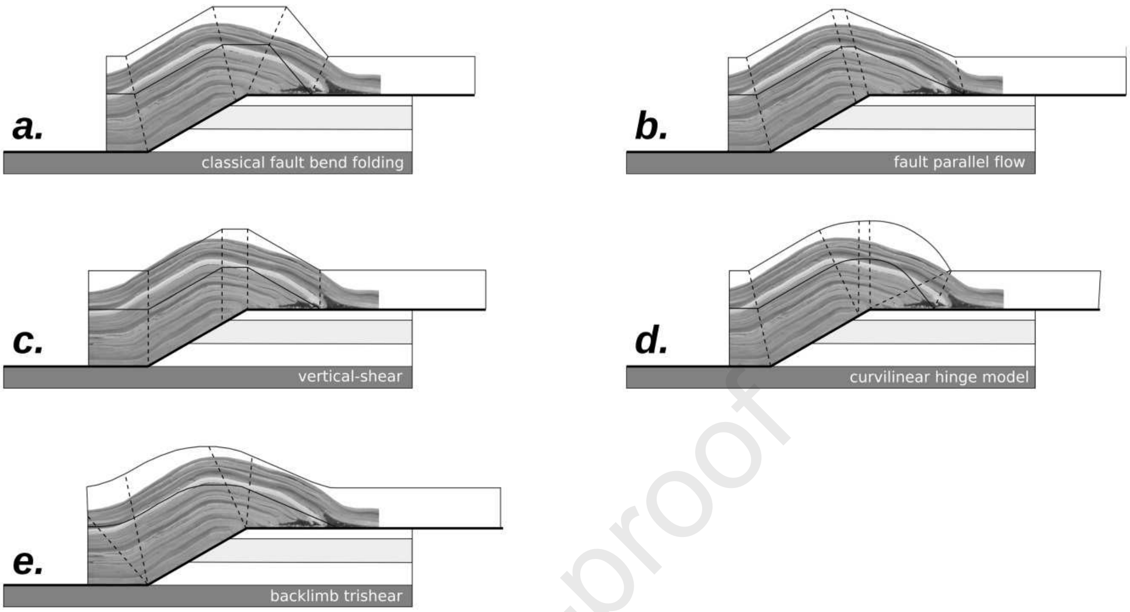
a.
classical fault bend folding
b.
fault parallel flow
c.
vertical-shear
d.
curvilinear hinge model
e.
backlimb trishear

Figure 5

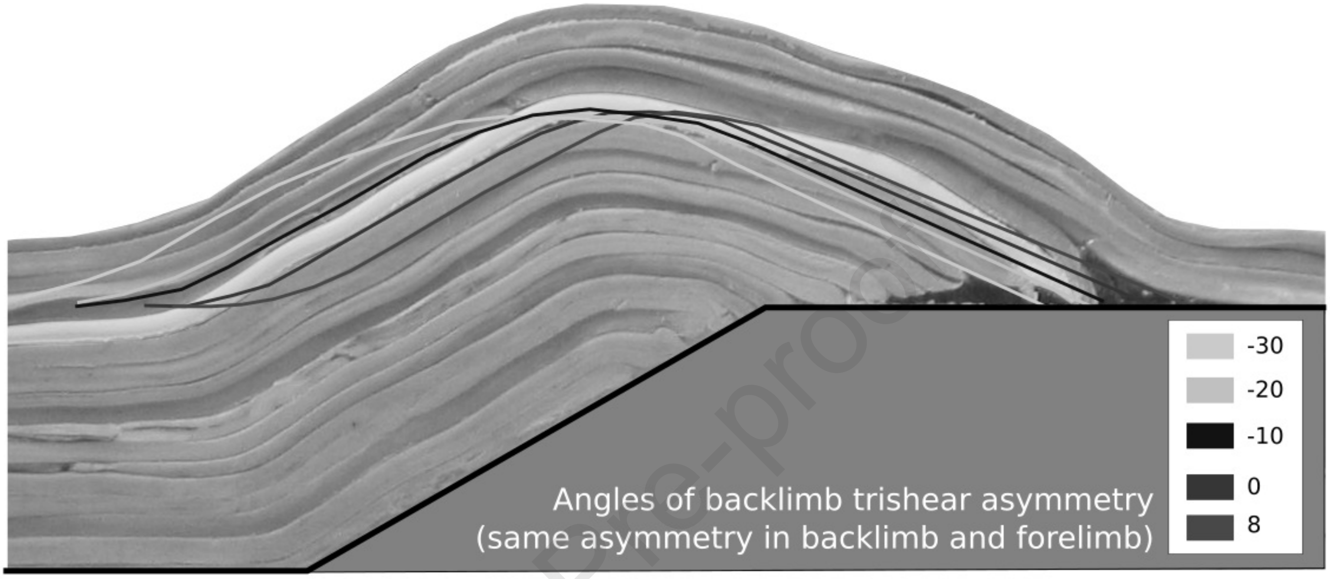
-30
-20
-10
0
8
Angles of backlimb trishear asymmetry
(same asymmetry in backlimb and forelimb)

Figure 6

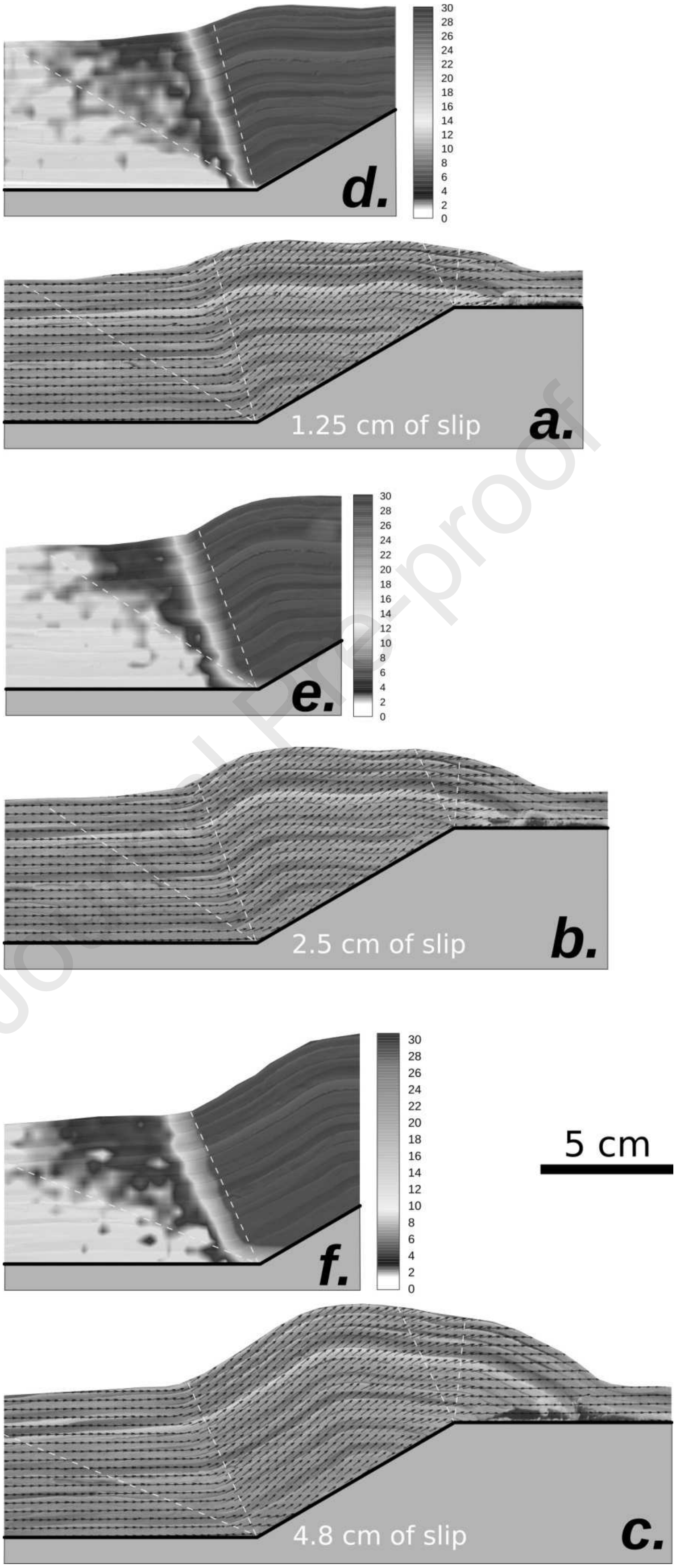
30
28
26
24
22
20
18
16
14
12
10
8
6
4
2
0
d.
1.25 cm of slip
a.
e.
2.5 cm of slip
b.
f.
5 cm
4.8 cm of slip
c.

Figure 7

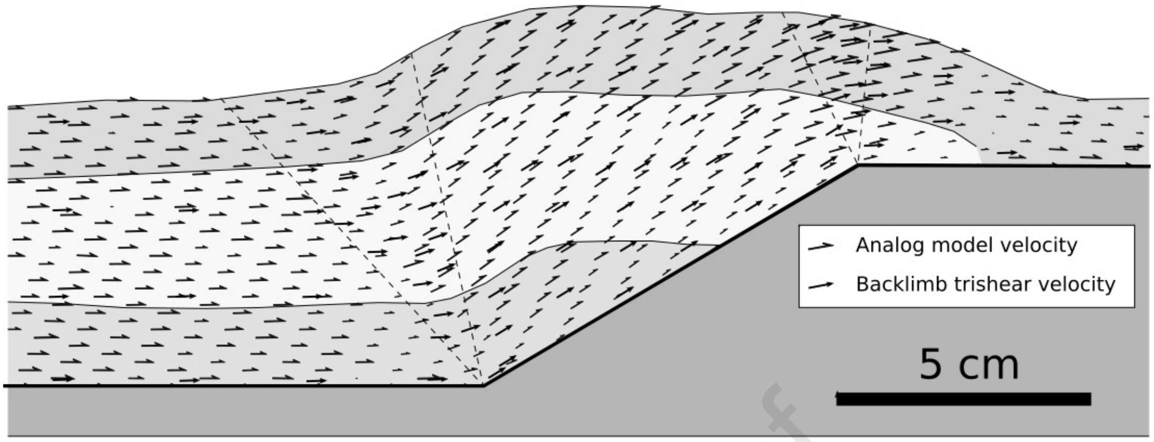

Figure 8

a.

Kinematic model	A (cm/h)	B (cm/h)	C (cm/h)
CFBF	6.8	6.8	3.9
FPF	6.8	6.8	6.8
ISh (vert.)	6.8	7.85	6.8
CH	6.8	6.8	3.9
BLT (-10;+8)	6.8	6.19	5.7

b.

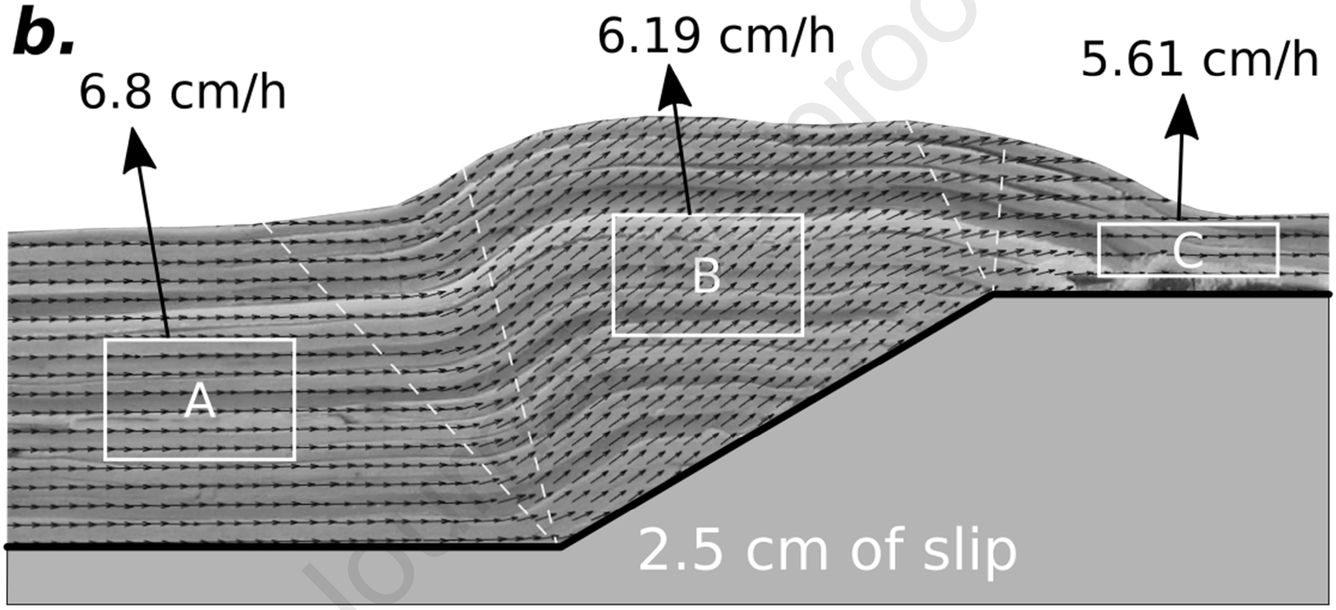

Figure 9

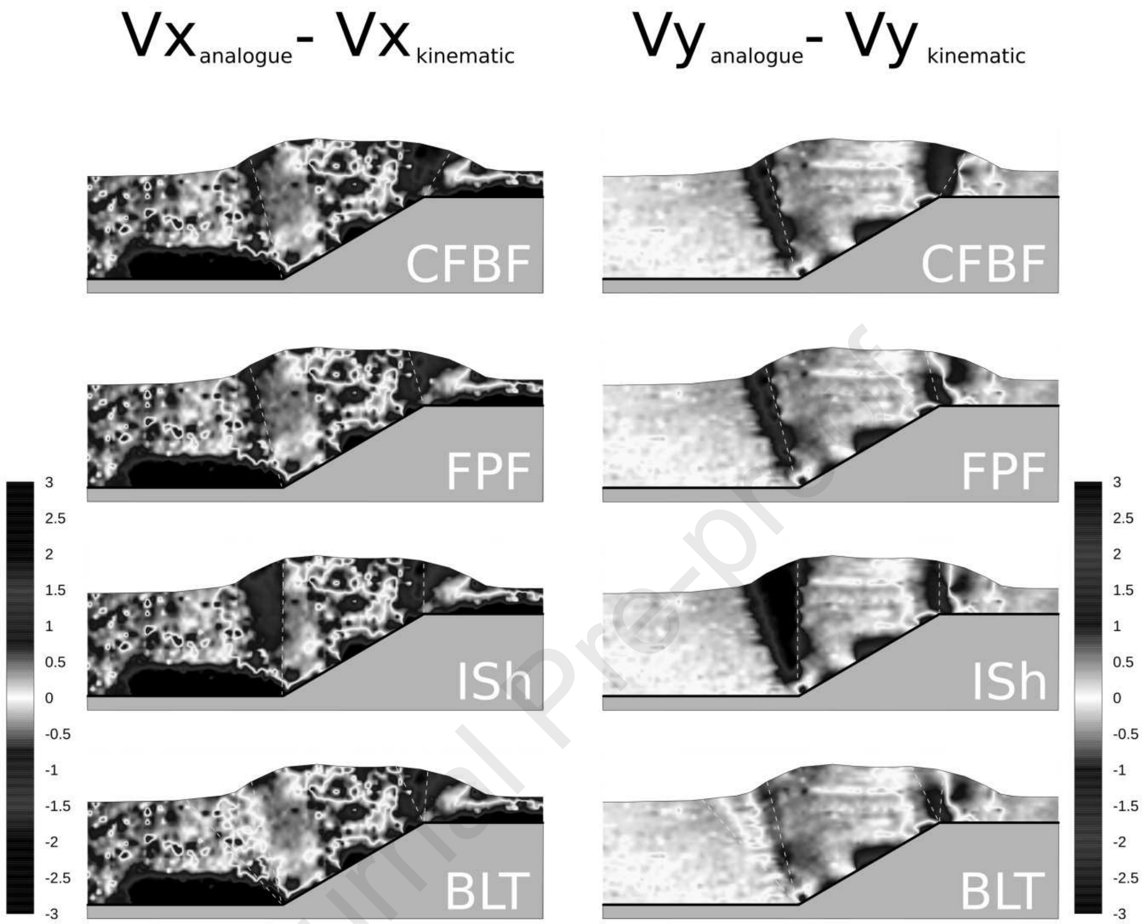
Vx analogue - Vx kinematic
Vy analogue - Vy kinematic
CFBF
FPF
ISh
BLT
CFBF
FPF
ISh
BLT
3
2.5
2
1.5
1
0.5
0
-0.5
-1
-1.5
-2
-2.5
-3

Figure 10

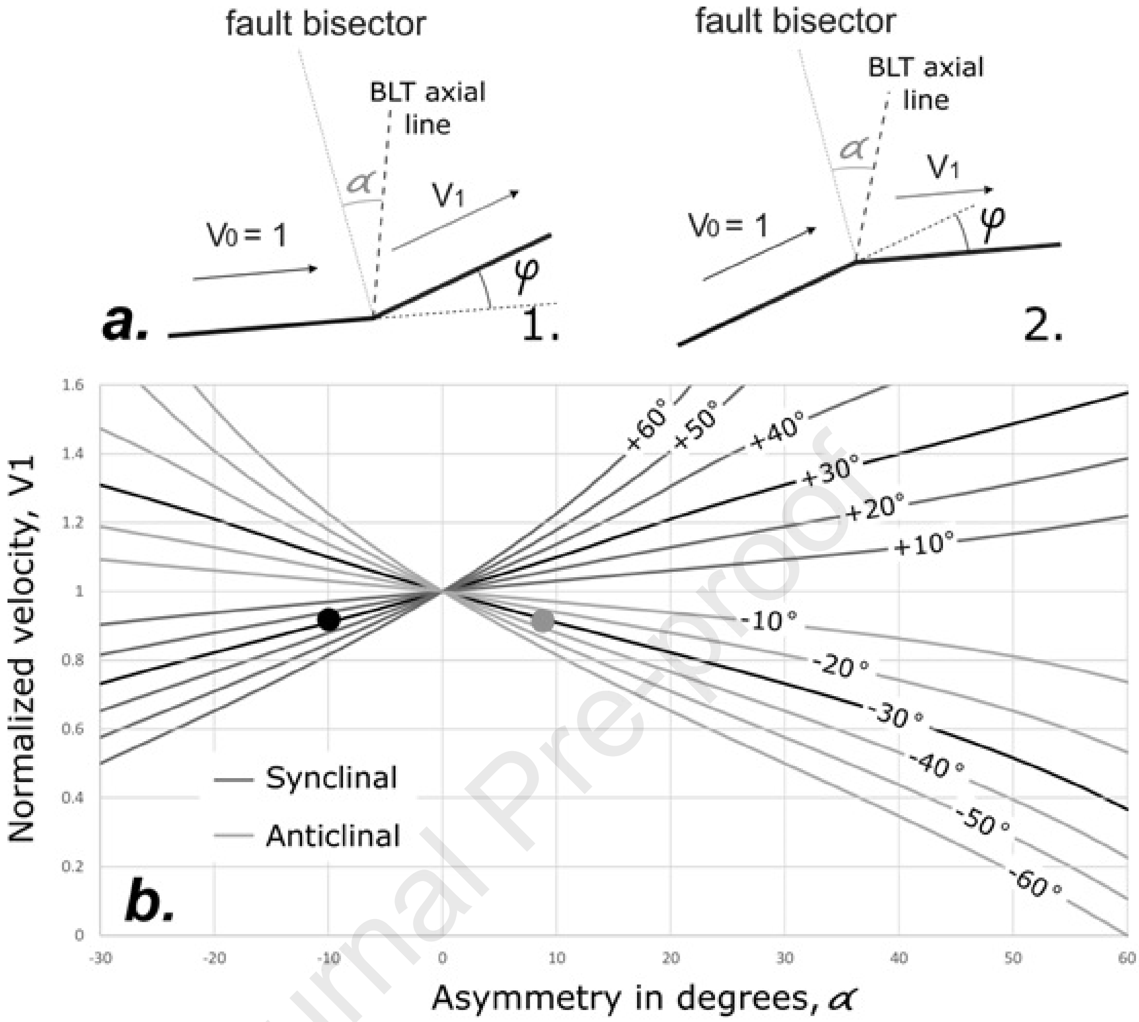
fault bisector
BLT axial line
α
V1
V0 = 1
φ
a.
1.
2.
+60°
+50°
+40°
+30°
+20°
+10°
-10°
-20°
-30°
-40°
-50°
-60°
Synclinal
Anticlinal
b.
Normalized velocity, V1
Asymmetry in degrees, α
1.6
1.4
1.2
1
0.8
0.6
0.4
0.2
0
-30
-20
-10
0
10
20
30
40
50
60

Figure 11

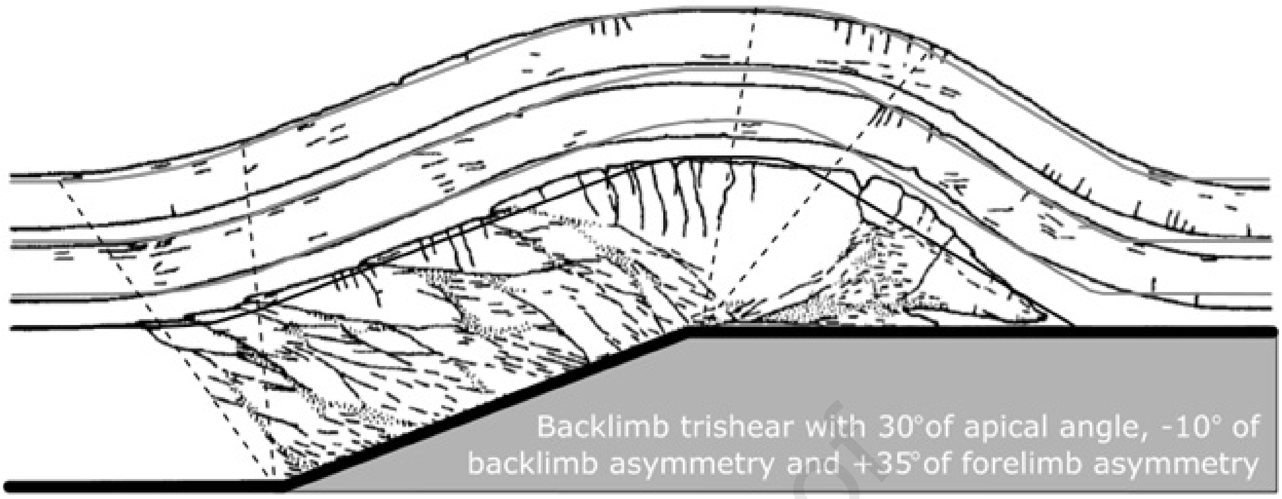
Backlimb trishear with 30°of apical angle, -10° of
backlimb asymmetry and +35°of forelimb asymmetry

Figure 12

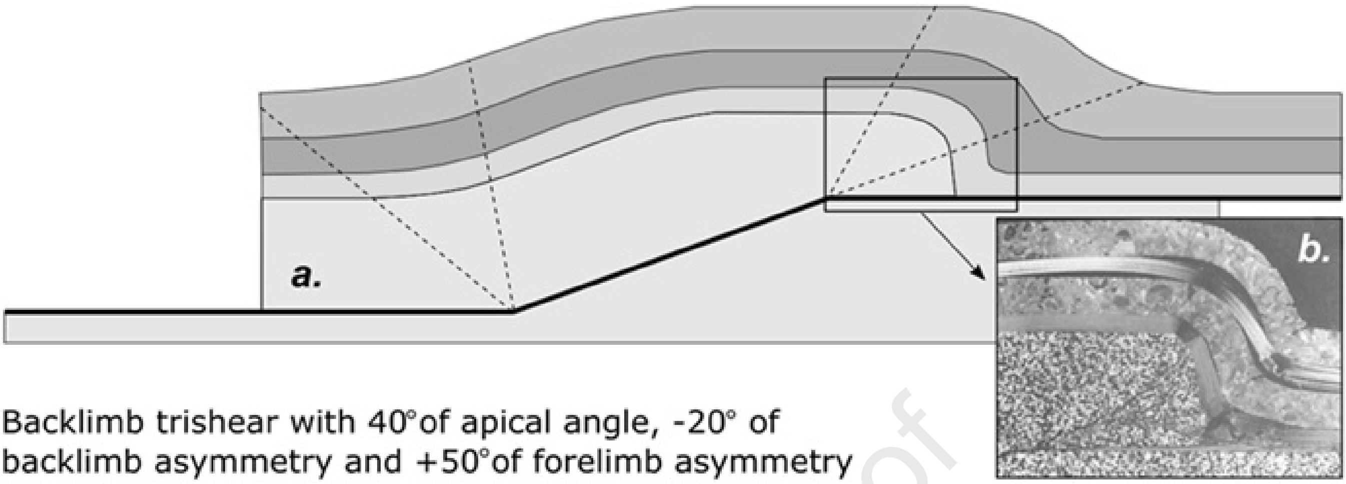

Backlimb trishear with 40° of apical angle, -20° of backlimb asymmetry and +50° of forelimb asymmetry

Highlights:

Analogue model was performed to obtain the velocity field during deformation.

Documentation of velocity vectors comes from particle image velocimetry.

Backlimb trishear can represent the geometry and directions of particles velocities.

Steeper-dipping forelimbs can be reproduced using high positive asymmetries.

Backlimb trishear apical angle can be used to control the shape of the hinges.

Declaration of interests

☒ The authors declare that they have no known competing financial interests or personal relationships that could have appeared to influence the work reported in this paper.

☐The authors declare the following financial interests/personal relationships which may be considered as potential competing interests: